



Measurement of J/ψ production in pp collisions at $\sqrt{s} = 7$ TeV

The LHCb Collaboration¹

Abstract

The production of J/ψ mesons in proton-proton collisions at $\sqrt{s} = 7$ TeV is studied with the LHCb detector at the LHC. The differential cross-section for prompt J/ψ production is measured as a function of the J/ψ transverse momentum p_T and rapidity y in the fiducial region $p_T \in [0; 14]$ GeV/ c and $y \in [2.0; 4.5]$. The differential cross-section and fraction of J/ψ from b -hadron decays are also measured in the same p_T and y ranges. The analysis is based on a data sample corresponding to an integrated luminosity of 5.2 pb^{-1} . The measured cross-sections integrated over the fiducial region are $10.52 \pm 0.04 \pm 1.40^{+1.64}_{-2.20} \mu\text{b}$ for prompt J/ψ production and $1.14 \pm 0.01 \pm 0.16 \mu\text{b}$ for J/ψ from b -hadron decays, where the first uncertainty is statistical and the second systematic. The prompt J/ψ production cross-section is obtained assuming no J/ψ polarisation and the third error indicates the acceptance uncertainty due to this assumption.

Keywords: charmonium, production, cross-section, LHC, LHCb

PACS numbers: 14.40.Pq, 13.60.Le

Submitted to Eur. Phys. J. C

¹Authors are listed on the following pages.

The LHCb Collaboration

R. Aaij²³, B. Adeva³⁶, M. Adinolfi⁴², C. Adrover⁶, A. Affolder⁴⁸, Z. Ajaltouni⁵, J. Albrecht³⁷, F. Alessio^{6,37}, M. Alexander⁴⁷, P. Alvarez Cartelle³⁶, A.A. Alves Jr²², S. Amato², Y. Amhis³⁸, J. Amoraal²³, J. Anderson³⁹, R.B. Appleby⁵⁰, O. Aquines Gutierrez¹⁰, L. Arrabito⁵³, M. Artuso⁵², E. Aslanides⁶, G. Auremma^{22,m}, S. Bachmann¹¹, D.S. Bailey⁵⁰, V. Balagura^{30,37}, W. Baldini¹⁶, R.J. Barlow⁵⁰, C. Barschel³⁷, S. Barsuk⁷, A. Bates⁴⁷, C. Bauer¹⁰, Th. Bauer²³, A. Bay³⁸, I. Bediaga¹, K. Belous³⁴, I. Belyaev^{30,37}, E. Ben-Haim⁸, M. Benayoun⁸, G. Bencivenni¹⁸, R. Bernet³⁹, M.-O. Bettler^{17,37}, M. van Beuzekom²³, S. Bifani¹², A. Bizzeti^{17,h}, P.M. Bjørnstad⁵⁰, T. Blake⁴⁹, F. Blanc³⁸, C. Blanks⁴⁹, J. Blouw¹¹, S. Blusk⁵², A. Bobrov³³, V. Bocci²², A. Bondar³³, N. Bondar^{29,37}, W. Bonivento¹⁵, S. Borghi⁴⁷, A. Borgia⁵², E. Bos²³, T.J.V. Bowcock⁴⁸, C. Bozzi¹⁶, T. Brambach⁹, J. van den Brand²⁴, J. Bressieux³⁸, S. Brisbane⁵¹, M. Britsch¹⁰, T. Britton⁵², N.H. Brook⁴², H. Brown⁴⁸, A. Büchler-Germann³⁹, A. Bursche³⁹, J. Buytaert³⁷, S. Cadeddu¹⁵, J.M. Caicedo Carvajal³⁷, O. Callot⁷, M. Calvi^{20,j}, M. Calvo Gomez^{35,n}, A. Camboni³⁵, P. Campana¹⁸, A. Carbone¹⁴, G. Carboni^{21,k}, R. Cardinale^{19,i}, A. Cardini¹⁵, L. Carson³⁶, K. Carvalho Akiba²³, G. Casse⁴⁸, M. Cattaneo³⁷, M. Charles⁵¹, Ph. Charpentier³⁷, N. Chiapolini³⁹, X. Cid Vidal³⁶, P.J. Clark⁴⁶, P.E.L. Clarke⁴⁶, M. Clemencic³⁷, H.V. Cliff⁴³, J. Closier³⁷, C. Coca²⁸, V. Coco²³, J. Cogan⁶, P. Collins³⁷, F. Constantin²⁸, G. Conti³⁸, A. Contu⁵¹, M. Coombes⁴², G. Corti³⁷, G.A. Cowan³⁸, R. Currie⁴⁶, B. D’Almagre⁷, C. D’Ambrosio³⁷, W. Da Silva⁸, P. David⁸, I. De Bonis⁴, S. De Capua^{21,k}, M. De Cian³⁹, F. De Lorenzi¹², J.M. De Miranda¹, L. De Paula², P. De Simone¹⁸, D. Decamp⁴, H. Degaudenzi^{38,37}, M. Deissenroth¹¹, L. Del Buono⁸, C. Deplano¹⁵, O. Deschamps⁵, F. Dettori^{15,d}, J. Dickens⁴³, H. Dijkstra³⁷, M. Dima²⁸, P. Diniz Batista¹, S. Donleavy⁴⁸, D. Dossett⁴⁴, A. Dovbnya⁴⁰, F. Dupertuis³⁸, R. Dzhelyadin³⁴, C. Eames⁴⁹, S. Easo⁴⁵, U. Egede⁴⁹, V. Egorychev³⁰, S. Eidelman³³, D. van Eijk²³, F. Eisele¹¹, S. Eisenhardt⁴⁶, L. Eklund⁴⁷, D.G. d’Enterria^{35,o}, D. Esperante Pereira³⁶, L. Estève⁴³, E. Fanchini^{20,j}, C. Färber¹¹, G. Fardell⁴⁶, C. Farinelli²³, S. Farry¹², V. Fave³⁸, V. Fernandez Albor³⁶, M. Ferro-Luzzi³⁷, S. Filippov³², C. Fitzpatrick⁴⁶, F. Fontanelli^{19,i}, R. Forty³⁷, M. Frank³⁷, C. Frei³⁷, M. Frosini^{17,f}, J.L. Fungueirino Pazos³⁶, S. Furcas²⁰, A. Gallas Torreira³⁶, D. Galli^{14,c}, M. Gandelman², P. Gandini⁵¹, Y. Gao³, J.-C. Garnier³⁷, J. Garofoli⁵², L. Garrido³⁵, C. Gaspar³⁷, N. Gauvin³⁸, M. Gersabeck³⁷, T. Gershon⁴⁴, Ph. Ghez⁴, V. Gibson⁴³, V.V. Gligorov³⁷, C. Göbel⁵⁴, D. Golubkov³⁰, A. Golutvin^{49,30,37}, A. Gomes², H. Gordon⁵¹, M. Grabalosa Gándara³⁵, R. Graciani Diaz³⁵, L.A. Granado Cardoso³⁷, E. Graugés³⁵, G. Graziani¹⁷, A. Grecu²⁸, S. Gregson⁴³, B. Gui⁵², E. Gushchin³², Yu. Guz^{34,37}, T. Gys³⁷, G. Haefeli³⁸, S.C. Haines⁴³, T. Hampson⁴², S. Hansmann-Menzemer¹¹, R. Harji⁴⁹, N. Harnew⁵¹, P.F. Harrison⁴⁴, J. He⁷, K. Hennessy⁴⁸, P. Henrard⁵, J.A. Hernando Morata³⁶, E. van Herwijnen³⁷, A. Hicheur³⁸, E. Hicks⁴⁸, W. Hofmann¹⁰, K. Holubyev¹¹, P. Hopchev⁴, W. Hulsbergen²³, P. Hunt⁵¹, T. Huse⁴⁸, R.S. Huston¹², D. Hutchcroft⁴⁸, V. Iakovenko^{7,41}, C. Iglesias Escudero³⁶, P. Ilten¹², J. Imong⁴², R. Jacobsson³⁷, M. Jahjah Hussein⁵, E. Jans²³, F. Jansen²³, P. Jaton³⁸, B. Jean-Marie⁷, F. Jing³, M. John⁵¹, D. Johnson⁵¹, C.R. Jones⁴³, B. Jost³⁷, F. Kapusta⁸, T.M. Karbach⁹, J. Keaveney¹², U. Kerzel³⁷, T. Ketel²⁴, A. Keune³⁸, B. Khanji⁶, Y.M. Kim⁴⁶, M. Knecht³⁸, S. Koblitz³⁷, A. Konoplyannikov³⁰, P. Koppenburg²³, A. Kozlinskiy²³, L. Kravchuk³², G. Krocker¹¹, P. Krokovny¹¹, F. Kruse⁹, K. Kruzelecki³⁷, M. Kucharczyk²⁵, S. Kukulak²⁵, R. Kumar^{14,37}, T. Kvaratskheliya³⁰, V.N. La Thi³⁸, D. Lacarrere³⁷, G. Lafferty⁵⁰, A. Lai¹⁵, R.W. Lambert³⁷, G. Lanfranchi¹⁸, C. Langenbruch¹¹, T. Latham⁴⁴, R. Le Gac⁶, J. van Leerdam²³, J.-P. Lees⁴, R. Lefèvre⁵, A. Leflat^{31,37}, J. Lefrançois⁷, O. Leroy⁶, T. Lesiak²⁵, L. Li³, Y.Y. Li⁴³, L. Li Gioi⁵, M. Lieng⁹, M. Liles⁴⁸, R. Lindner³⁷, C. Linn¹¹, B. Liu³, G. Liu³⁷, J.H. Lopes², E. Lopez Asamar³⁵, N. Lopez-March³⁸, J. Luisier³⁸, B. M’charek²⁴, F. Machefert⁷, I.V. Machikhiliyan^{4,30}, F. Maciuc¹⁰, O. Maev²⁹, J. Magnin¹, A. Maier³⁷, S. Malde⁵¹, R.M.D. Mamunur³⁷, G. Manca^{15,d,37}, G. Mancinelli⁶, N. Mangiafave⁴³, U. Marconi¹⁴, R. Märki³⁸, J. Marks¹¹, G. Martellotti²², A. Martens⁷, L. Martin⁵¹, A. Martín Sánchez⁷, D. Martinez Santos³⁷, A. Massafferri¹, Z. Mathe¹², C. Matteuzzi²⁰, M. Matveev²⁹, V. Matveev³⁴, E. Maurice⁶, B. Maynard⁵², A. Mazurov³², G. McGregor⁵⁰, R. McNulty¹², C. Mclean⁴⁶, M. Meissner¹¹, M. Merk²³, J. Merkel⁹, M. Merkin³¹, R. Messi^{21,k}, S. Miglioranza³⁷, D.A. Milanes¹³, M.-N. Minard⁴, S. Monteil⁵, D. Moran¹², P. Morawski²⁵, J.V. Morris⁴⁵, R. Mountain⁵², I. Mous²³, F. Muheim⁴⁶, K. Müller³⁹, R. Muresan^{28,38}, F. Murtas¹⁸, B. Muryn²⁶, M. Musy³⁵, J. Mylroie-Smith⁴⁸, P. Naik⁴², T. Nakada³⁸, R. Nandakumar⁴⁵, J. Nardulli⁴⁵, M. Nedos⁹, M. Needham⁴⁶, N. Neufeld³⁷, M. Nicol⁷, S. Nies⁹, V. Niess⁵, N. Nikitin³¹, A. Oblakowska-Mucha²⁶, V. Obraztsov³⁴, S. Oggero²³, O. Okhrimenko⁴¹, R. Oldeman^{15,d}, M. Orlandea²⁸, A. Ostankov³⁴, B. Pal⁵², J. Palacios³⁹, M. Palutan¹⁸, J. Panman³⁷, A. Papanestis⁴⁵, M. Pappagallo^{13,b}, C. Parkes^{47,37}, C.J. Parkinson⁴⁹, G. Passaleva¹⁷, G.D. Patel⁴⁸, M. Patel⁴⁹,

S.K. Paterson^{49,37}, G.N. Patrick⁴⁵, C. Patrignani^{19,i}, C. Pavel-Nicorescu²⁸, A. Pazos Alvarez³⁶, A. Pellegrino²³, G. Penso^{22,l}, M. Pepe Altarelli³⁷, S. Perazzini^{14,c}, D.L. Perego^{20,j}, E. Perez Trigo³⁶, A. Pérez-Calero Yzquierdo³⁵, P. Perret⁵, A. Petrella^{16,e,37}, A. Petrolini^{19,i}, B. Pie Valls³⁵, B. Pietrzyk⁴, D. Pinci²², R. Plackett⁴⁷, S. Playfer⁴⁶, M. Plo Casasus³⁶, G. Polok²⁵, A. Poluektov^{44,33}, E. Polcarpo², D. Popov¹⁰, B. Popovici²⁸, C. Potterat³⁸, A. Powell⁵¹, T. du Pree²³, V. Pugatch⁴¹, A. Puig Navarro³⁵, W. Qian³, J.H. Rademacker⁴², B. Rakotomiramanana³⁸, I. Raniuk⁴⁰, G. Raven²⁴, S. Redford⁵¹, W. Reece⁴⁹, A.C. dos Reis¹, S. Ricciardi⁴⁵, K. Rinnert⁴⁸, D.A. Roa Romero⁵, P. Robbe^{7,37}, E. Rodrigues⁴⁷, F. Rodrigues², C. Rodriguez Cobo³⁶, P. Rodriguez Perez³⁶, G.J. Rogers⁴³, V. Romanovsky³⁴, J. Rouvinet³⁸, T. Ruf⁵⁷, H. Ruiz³⁵, G. Sabatino^{21,k}, J.J. Saborido Silva³⁶, N. Sagidova²⁹, P. Sail⁴⁷, B. Saitta^{15,d}, C. Salzmann³⁹, A. Sambade Varela³⁷, M. Sannino^{19,i}, R. Santacesaria²², R. Santinelli³⁷, E. Santovetti^{21,k}, M. Sapunov⁶, A. Sarti¹⁸, C. Satriano^{22,m}, A. Satta²¹, M. Savrie^{16,e}, D. Savrina³⁰, P. Schaack⁴⁹, M. Schiller¹¹, S. Schleich⁹, M. Schmelling¹⁰, B. Schmidt³⁷, O. Schneider³⁸, A. Schopper³⁷, M.-H. Schune⁷, R. Schwemmer³⁷, A. Sciubba^{18,l}, M. Seco³⁶, A. Semennikov³⁰, K. Senderowska²⁶, N. Serra²³, J. Serrano⁶, B. Shao³, M. Shapkin³⁴, I. Shapoval^{40,37}, P. Shatalov³⁰, Y. Shcheglov²⁹, T. Shears⁴⁸, L. Shekhtman³³, O. Shevchenko⁴⁰, V. Shevchenko³⁰, A. Shires⁴⁹, E. Simioni²⁴, H.P. Skottowe⁴³, T. Skwarnicki⁵², A.C. Smith³⁷, K. Sobczak⁵, F.J.P. Soler⁴⁷, A. Solomin⁴², P. Somogy³⁷, F. Soomro⁴⁹, B. Souza De Paula², B. Spaan⁹, A. Sparkes⁴⁶, E. Spiridenkov²⁹, P. Spradlin⁵¹, F. Stagni³⁷, O. Steinkamp³⁹, O. Stenyakin³⁴, S. Stoica²⁸, S. Stone⁵², B. Storaci²³, U. Straumann³⁹, N. Styles⁴⁶, M. Szczekowski²⁷, P. Szczypka³⁸, T. Szumlak²⁶, S. T'Jampens⁴, V. Talanov³⁴, E. Teodorescu²⁸, H. Terrier²³, F. Teubert³⁷, C. Thomas^{51,45}, E. Thomas³⁷, J. van Tilburg³⁹, V. Tisserand⁴, M. Tobin³⁹, S. Topp-Joergensen⁵¹, M.T. Tran³⁸, A. Tsaregorodtsev⁶, N. Tuning²³, A. Ukleja²⁷, P. Urquijo⁵², U. Uwer¹¹, V. Vagnoni¹⁴, G. Valenti¹⁴, R. Vazquez Gomez³⁵, P. Vazquez Regueiro³⁶, S. Vecchi¹⁶, J.J. Velthuis⁴², M. Veltri^{17,g}, K. Vervink³⁷, B. Viaud⁷, I. Videau⁷, X. Vilasis-Cardona^{35,n}, J. Visniakov³⁶, A. Vollhardt³⁹, D. Voong⁴², A. Vorobyev²⁹, An. Vorobyev²⁹, H. Voss¹⁰, K. Wacker⁹, S. Wandernoth¹¹, J. Wang⁵², D.R. Ward⁴³, A.D. Webber⁵⁰, D. Websdale⁴⁹, M. Whitehead⁴⁴, D. Wiedner¹¹, L. Wiggers²³, G. Wilkinson⁵¹, M.P. Williams^{44,45}, M. Williams⁴⁹, F.F. Wilson⁴⁵, J. Wishahi⁹, M. Witek²⁵, W. Witzeling³⁷, S.A. Wotton⁴³, K. Wyllie³⁷, Y. Xie⁴⁶, F. Xing⁵¹, Z. Yang³, G. Ybeles Smit²³, R. Young⁴⁶, O. Yushchenko³⁴, M. Zavertyaev^{10,a}, L. Zhang⁵², W.C. Zhang¹², Y. Zhang³, A. Zhelezov¹¹, L. Zhong³, E. Zverev³¹.

¹Centro Brasileiro de Pesquisas Físicas (CBPF), Rio de Janeiro, Brazil

²Universidade Federal do Rio de Janeiro (UFRJ), Rio de Janeiro, Brazil

³Center for High Energy Physics, Tsinghua University, Beijing, China

⁴LAPP, Université de Savoie, CNRS/IN2P3, Annecy-Le-Vieux, France

⁵Clermont Université, Université Blaise Pascal, CNRS/IN2P3, LPC, Clermont-Ferrand, France

⁶CPPM, Aix-Marseille Université, CNRS/IN2P3, Marseille, France

⁷LAL, Université Paris-Sud, CNRS/IN2P3, Orsay, France

⁸LPNHE, Université Pierre et Marie Curie, Université Paris Diderot, CNRS/IN2P3, Paris, France

⁹Fakultät Physik, Technische Universität Dortmund, Dortmund, Germany

¹⁰Max-Planck-Institut für Kernphysik (MPIK), Heidelberg, Germany

¹¹Physikalisches Institut, Ruprecht-Karls-Universität Heidelberg, Heidelberg, Germany

¹²School of Physics, University College Dublin, Dublin, Ireland

¹³Sezione INFN di Bari, Bari, Italy

¹⁴Sezione INFN di Bologna, Bologna, Italy

¹⁵Sezione INFN di Cagliari, Cagliari, Italy

¹⁶Sezione INFN di Ferrara, Ferrara, Italy

¹⁷Sezione INFN di Firenze, Firenze, Italy

¹⁸Laboratori Nazionali dell'INFN di Frascati, Frascati, Italy

¹⁹Sezione INFN di Genova, Genova, Italy

²⁰Sezione INFN di Milano Bicocca, Milano, Italy

²¹Sezione INFN di Roma Tor Vergata, Roma, Italy

²²Sezione INFN di Roma Sapienza, Roma, Italy

²³Nikhef National Institute for Subatomic Physics, Amsterdam, Netherlands

²⁴Nikhef National Institute for Subatomic Physics and Vrije Universiteit, Amsterdam, Netherlands

²⁵Henryk Niewodniczanski Institute of Nuclear Physics Polish Academy of Sciences, Cracow, Poland

²⁶Faculty of Physics & Applied Computer Science, Cracow, Poland

²⁷Soltan Institute for Nuclear Studies, Warsaw, Poland

- ²⁸*Horia Hulubei National Institute of Physics and Nuclear Engineering, Bucharest-Magurele, Romania*
- ²⁹*Petersburg Nuclear Physics Institute (PNPI), Gatchina, Russia*
- ³⁰*Institute of Theoretical and Experimental Physics (ITEP), Moscow, Russia*
- ³¹*Institute of Nuclear Physics, Moscow State University (SINP MSU), Moscow, Russia*
- ³²*Institute for Nuclear Research of the Russian Academy of Sciences (INR RAN), Moscow, Russia*
- ³³*Budker Institute of Nuclear Physics (BINP), Novosibirsk, Russia*
- ³⁴*Institute for High Energy Physics (IHEP), Protvino, Russia*
- ³⁵*Universitat de Barcelona, Barcelona, Spain*
- ³⁶*Universidad de Santiago de Compostela, Santiago de Compostela, Spain*
- ³⁷*European Organization for Nuclear Research (CERN), Geneva, Switzerland*
- ³⁸*Ecole Polytechnique Fédérale de Lausanne (EPFL), Lausanne, Switzerland*
- ³⁹*Physik-Institut, Universität Zürich, Zürich, Switzerland*
- ⁴⁰*NSC Kharkiv Institute of Physics and Technology (NSC KIPT), Kharkiv, Ukraine*
- ⁴¹*Institute for Nuclear Research of the National Academy of Sciences (KINR), Kyiv, Ukraine*
- ⁴²*H.H. Wills Physics Laboratory, University of Bristol, Bristol, United Kingdom*
- ⁴³*Cavendish Laboratory, University of Cambridge, Cambridge, United Kingdom*
- ⁴⁴*Department of Physics, University of Warwick, Coventry, United Kingdom*
- ⁴⁵*STFC Rutherford Appleton Laboratory, Didcot, United Kingdom*
- ⁴⁶*School of Physics and Astronomy, University of Edinburgh, Edinburgh, United Kingdom*
- ⁴⁷*School of Physics and Astronomy, University of Glasgow, Glasgow, United Kingdom*
- ⁴⁸*Oliver Lodge Laboratory, University of Liverpool, Liverpool, United Kingdom*
- ⁴⁹*Imperial College London, London, United Kingdom*
- ⁵⁰*School of Physics and Astronomy, University of Manchester, Manchester, United Kingdom*
- ⁵¹*Department of Physics, University of Oxford, Oxford, United Kingdom*
- ⁵²*Syracuse University, Syracuse, NY, United States of America*
- ⁵³*CC-IN2P3, CNRS/IN2P3, Lyon-Villeurbanne, France, associated member*
- ⁵⁴*Pontifícia Universidade Católica do Rio de Janeiro (PUC-Rio), Rio de Janeiro, Brazil, associated to ²*

^a*P.N. Lebedev Physical Institute, Russian Academy of Science (LPI RAS), Moscow, Russia*

^b*Università di Bari, Bari, Italy*

^c*Università di Bologna, Bologna, Italy*

^d*Università di Cagliari, Cagliari, Italy*

^e*Università di Ferrara, Ferrara, Italy*

^f*Università di Firenze, Firenze, Italy*

^g*Università di Urbino, Urbino, Italy*

^h*Università di Modena e Reggio Emilia, Modena, Italy*

ⁱ*Università di Genova, Genova, Italy*

^j*Università di Milano Bicocca, Milano, Italy*

^k*Università di Roma Tor Vergata, Roma, Italy*

^l*Università di Roma La Sapienza, Roma, Italy*

^m*Università della Basilicata, Potenza, Italy*

ⁿ*LIFAELS, La Salle, Universitat Ramon Llull, Barcelona, Spain*

^o*Institució Catalana de Recerca i Estudis Avançats (ICREA), Barcelona, Spain*

1 Introduction

Understanding J/ψ meson hadroproduction has been a long-term effort both experimentally and theoretically. However, despite the considerable progress made in recent years [1], none of the existing theoretical models can successfully describe both the transverse momentum (p_T) dependence of the J/ψ cross-section and the J/ψ polarisation measured at the Tevatron. The colour-singlet model (CSM) at leading order in α_s [2] underestimates J/ψ production by two orders of magnitude [3], and even more at high p_T . Including additional processes, such as quark and gluon fragmentation [4] leads to a better description of the p_T shape at high p_T , but still fails to reproduce the measured production rates. Computations performed in the framework of nonrelativistic quantum chromodynamics (NRQCD), where the $c\bar{c}$ pair can be produced in a colour-octet state [5], can explain the shape and the magnitude of the measured J/ψ cross-section. However, they predict a substantial transverse component for the polarisation of J/ψ mesons at large p_T . This is in disagreement with the CDF J/ψ polarisation measurement [6], casting doubt on the conclusion that the colour-octet terms dominate J/ψ production. More recent theoretical studies have considered the addition of the $gg \rightarrow J/\psi c\bar{c}$ process to the CSM [7, 8], or higher order corrections in α_s : $gg \rightarrow J/\psi gg$ [9] and $gg \rightarrow J/\psi ggg$ [10, 11]. With these additions, the discrepancy between theoretical predictions and experimental measurements significantly decreases. However, the agreement is still not perfect, leaving open the question of a complete description of J/ψ hadroproduction. The large rate of J/ψ production at the Large Hadron Collider (LHC) opens the door to new analyses that extend the phase-space region explored so far, such as that recently made by the CMS collaboration [12]. In particular, the LHCb detector provides the possibility to extend the measurements to the forward rapidity region.

Three sources of J/ψ production in pp collisions need to be considered when comparing experimental observables and theoretical calculations: direct J/ψ production, feed-down J/ψ from the decay of other heavier prompt charmonium states like χ_{c1} , χ_{c2} or $\psi(2S)$, and J/ψ from b -hadron decay chains. The sum of the first two sources will be called “prompt J/ψ ” in the following. The third source will be abbreviated as “ J/ψ from b ”.

This paper presents the measurement of the differential production cross-section of both prompt J/ψ and J/ψ from b as a function of the J/ψ transverse momentum and rapidity (y) with respect to the beam axis in the fiducial region $p_T \in [0; 14]$ GeV/ c and $y \in [2.0; 4.5]$. The effect due to the unknown J/ψ polarisation is estimated by providing results for the differential cross-sections for three extreme polarisation cases. The analysis of a larger data sample is needed to measure the J/ψ polarisation over the kinematic range considered.

2 The LHCb detector, data sample and Monte Carlo simulation

The LHCb detector is a forward spectrometer described in detail in Ref. [13]. The detector elements are placed along the beam line of the LHC starting with the Vertex Locator (VELO), a silicon strip device that surrounds the pp interaction region and is positioned with its sensitive area 8 mm from the beam during collisions. The VELO provides precise measurements of the positions of the primary pp interaction vertices and decay vertices of long-lived hadrons, and contributes to the measurement of track momenta. Other detectors used to measure track momenta are a large area silicon strip detector located before a 4 Tm dipole magnet and a com-

bination of silicon strip detectors and straw drift chambers placed after it. Two Ring Imaging Cherenkov detectors are used to identify charged hadrons. Further downstream an Electromagnetic Calorimeter system (ECAL, Preshower – PRS – and Scintillating Pad Detector – SPD) is used for photon detection and electron identification, followed by a Hadron Calorimeter (HCAL). The muon detection consists of five muon stations (MUON) equipped with multi-wire proportional chambers, with the exception of the centre of the first station, which uses triple-GEM detectors. For the data included in this analysis all detector components were fully operational and in a stable condition and the main component of the dipole field was pointing upwards.

The LHCb trigger system consists of two levels. The first level (L0), implemented in hardware, is designed to reduce the LHC bunch crossing frequency of 40 MHz to a maximum of 1 MHz, at which the complete detector is read out. The ECAL, HCAL and MUON provide the capability of first-level hardware triggering. The second level is a software trigger (High Level Trigger, HLT) which runs on an event-filter farm and is implemented in two stages. HLT1 performs a partial event reconstruction to confirm the L0 trigger decision, and HLT2 performs a full event reconstruction to further discriminate signal events.

The study reported here uses data corresponding to an integrated luminosity of 5.2 pb^{-1} of pp collisions produced by the LHC at a centre-of-mass energy of 7 TeV in September 2010, with at maximum 1.6 MHz collision frequency. The data were collected using two L0 trigger lines: the single-muon line, which requires one muon candidate with a p_T larger than $1.4 \text{ GeV}/c$, and the dimuon line, which requires two muon candidates with p_T larger than $0.56 \text{ GeV}/c$ and $0.48 \text{ GeV}/c$, respectively. They provide the input candidates for the corresponding HLT1 lines: the first one confirms the single-muon candidates from L0, and applies a harder p_T selection at $1.8 \text{ GeV}/c$; the second line confirms the dimuon candidates and requires their combined mass to be greater than $2.5 \text{ GeV}/c^2$. The HLT2 algorithm selects events having two opposite charged muon candidates with an invariant mass greater than $2.9 \text{ GeV}/c^2$. For a fraction of the data, corresponding to an integrated luminosity of 3.0 pb^{-1} , the HLT1 single muon line was pre-scaled by a factor of five. The trigger efficiency is measured independently for the pre-scaled data set and for the rest of the sample, and the results subsequently combined.

To avoid the possibility that a few events with a high occupancy dominate the HLT CPU time, a set of global event cuts (GEC) is applied on the hit multiplicities of each sub-detector used by the pattern recognition algorithms. These cuts were introduced to cope with conditions encountered during the 2010 running period of the LHC, in which the average number of visible interactions per bunch crossing was equal to 1.8 for the data used for this analysis, a factor of five above the design value, at a time when only one fifth of the event-filter farm was installed. The GEC were chosen to reject busy events with a large number of pile-up interactions with minimal loss of luminosity. The average number of reconstructed primary vertices in selected and triggered events after GEC is equal to 2.1.

The Monte Carlo samples used for this analysis are based on the PYTHIA 6.4 generator [14] configured with the parameters detailed in Ref. [15]. The EvtGen package [16] was used to generate hadron decays, in particular J/ψ and b -hadrons, and the GEANT4 package [17] for the detector simulation. The prompt charmonium production processes activated in PYTHIA are those from the leading-order colour-singlet and colour-octet mechanisms. The b -hadron production in PYTHIA is based on leading order $2 \rightarrow 2$ QCD processes: $q\bar{q} \rightarrow q'\bar{q}'$, $qq' \rightarrow qq'$, $q\bar{q} \rightarrow gg$, $qg \rightarrow qg$, $gg \rightarrow q\bar{q}$ and $gg \rightarrow gg$. QED radiative corrections to the decay $J/\psi \rightarrow \mu^+\mu^-$ are generated using the PHOTOS package [18].

3 J/ψ selection

The analysis selects events in which at least one primary vertex is reconstructed from at least five charged tracks seen in the VELO. J/ψ candidates are formed from pairs of opposite sign tracks reconstructed in the full tracking system. Each track must have p_T above $0.7 \text{ GeV}/c$, have a good quality of the track fit ($\chi^2/\text{ndf} < 4$) and be identified as a muon by ensuring that it penetrates the iron of the MUON system. The two muons are required to originate from a common vertex, and only candidates with a χ^2 probability of the vertex fit larger than 0.5% are kept. Some charged particles can be reconstructed as more than one track. Duplicate tracks, which share too many hits with another track or are too close to another track, are removed.

J/ψ from b tend to be produced away from the primary vertex and can be separated from prompt J/ψ , which are produced at the primary vertex, by exploiting the J/ψ pseudo-proper time defined as

$$t_z = \frac{(z_{J/\psi} - z_{PV}) \times M_{J/\psi}}{p_z}, \quad (1)$$

where $z_{J/\psi}$ and z_{PV} are the positions along the z -axis (defined along the beam axis, and oriented from the VELO to the MUON) of the J/ψ decay vertex and of the primary vertex; p_z is the measured J/ψ momentum in the z direction and $M_{J/\psi}$ the nominal J/ψ mass. Given that b -hadrons are not fully reconstructed, the J/ψ momentum is used instead of the exact b -hadron momentum and the t_z variable provides a good estimate of the b -hadron decay proper time. For events with several primary vertices (68% of the events), the one which is closest to the J/ψ vertex in the z direction is selected.

4 Cross-section determination

The differential cross-section for J/ψ production in a given (p_T, y) bin is defined as

$$\frac{d^2\sigma}{dy dp_T} = \frac{N(J/\psi \rightarrow \mu^+\mu^-)}{\mathcal{L} \times \epsilon_{\text{tot}} \times \mathcal{B}(J/\psi \rightarrow \mu^+\mu^-) \times \Delta y \times \Delta p_T}, \quad (2)$$

where $N(J/\psi \rightarrow \mu^+\mu^-)$ is the number of observed $J/\psi \rightarrow \mu^+\mu^-$ in bin (p_T, y) , ϵ_{tot} the J/ψ detection efficiency including acceptance and trigger efficiency in bin (p_T, y) , \mathcal{L} the integrated luminosity, $\mathcal{B}(J/\psi \rightarrow \mu^+\mu^-)$ the branching fraction of the $J/\psi \rightarrow \mu^+\mu^-$ decay ($(5.93 \pm 0.06) \times 10^{-2}$ [19]), and $\Delta y = 0.5$ and $\Delta p_T = 1 \text{ GeV}/c$ the y and p_T bin sizes, respectively. The transverse momentum is defined as $p_T = \sqrt{p_x^2 + p_y^2}$ and the rapidity is defined as $y = \frac{1}{2} \ln \frac{E + p_z}{E - p_z}$ where (E, \mathbf{p}) is the J/ψ four-momentum in the centre-of-mass frame of the colliding protons.

In each bin of p_T and y , the fraction of signal J/ψ from all sources, $f_{J/\psi}$, is estimated from an extended unbinned maximum likelihood fit to the invariant mass distribution of the reconstructed J/ψ candidates in the interval $M_{\mu\mu} \in [2.95; 3.30] \text{ GeV}/c^2$, where the signal is described by a Crystal Ball function [20] and the combinatorial background by an exponential function. The fraction of J/ψ from b is then extracted from a fit to the t_z distribution.

As an example, Fig. 1 (left) shows the mass distribution together with the fit results for one specific bin ($3 < p_T < 4 \text{ GeV}/c$, $2.5 < y < 3.0$); the fit gives a mass resolution of $12.3 \pm 0.1 \text{ MeV}/c^2$ and a mean of $3095.3 \pm 0.1 \text{ MeV}/c^2$, where the errors are statistical only. The mass

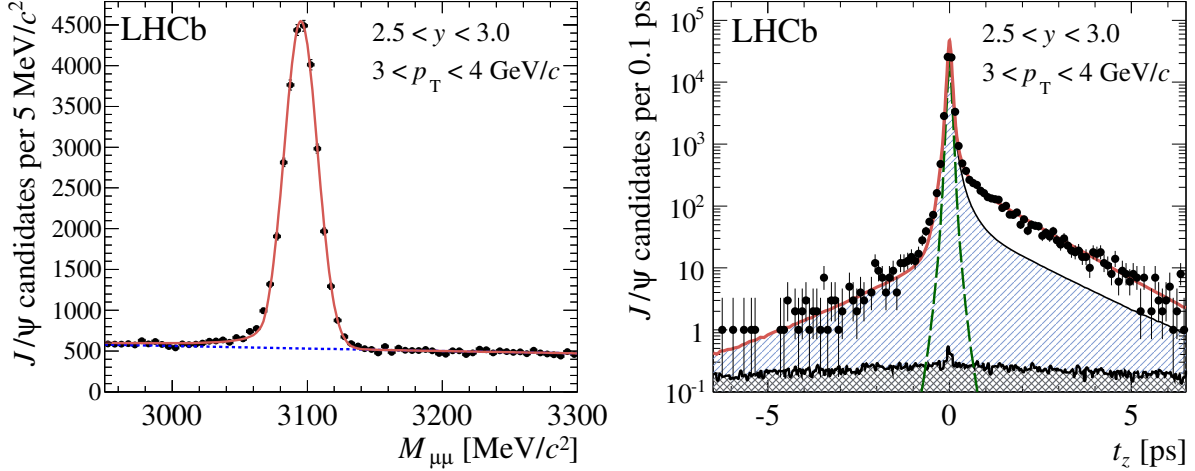


Figure 1: Dimuon mass distribution (*left*) and t_z distribution (*right*), with fit results superimposed, for one bin ($3 < p_T < 4 \text{ GeV}/c$, $2.5 < y < 3.0$). On the mass distribution, the *solid red line* is the total fit function, where the signal is described by a Crystal Ball function, and the *dashed blue line* represents the exponential background function. On the t_z distribution, the *solid red line* is the total fit function described in the text, the *green dashed line* is the prompt J/ψ contribution, the *single-hatched area* is the background component and the *cross-hatched area* is the tail contribution.

value is close to the known J/ψ mass value of $3096.916 \pm 0.011 \text{ MeV}/c^2$ [19], reflecting the current status of the mass-scale calibration; the difference between the two values has no effect on the results obtained in this analysis. Summing over all bins, a total signal yield of 565 000 events is obtained.

4.1 Determination of the fraction of J/ψ from b

The fraction of J/ψ from b , F_b , is determined from the fits to the pseudo-proper time t_z and the $\mu^+\mu^-$ invariant mass in each bin of p_T and y . The signal proper-time distribution is described by a delta function at $t_z = 0$ for the prompt J/ψ component, an exponential decay function for the J/ψ from b component and a long tail arising from the association of the J/ψ candidate with the wrong primary vertex. There are two main reasons for the wrong association:

1. Two or more primary vertices are close to each other and a primary vertex is reconstructed with tracks belonging to the different vertices, at a position that is different from the true primary vertex position.
2. The primary vertex from which the J/ψ originates is not found because too few tracks originating from the vertex are reconstructed, as confirmed by the simulation; the J/ψ candidate is then wrongly associated with another primary vertex found in the event.

In the first case, the positions of the reconstructed and of the true primary vertices are correlated. This category of events is distributed around $t_z = 0$ for the prompt component, with a width larger than the t_z distribution for correctly associated primary vertices. The contribution of these events to the t_z distribution is included in the resolution function described below.

The long tail is predominantly composed of events in the second category. Since the tail distribution affects the measurement of the J/ψ from b component, a method has been developed

to extract its shape from data. The method consists of associating a J/ψ from a given event with the primary vertex of the next event in the J/ψ sample. This simulates the position of an uncorrelated primary vertex with which the J/ψ is associated. The shape of the tail contribution to the signal t_z distribution is then obtained from the distribution of

$$t_z^{\text{next}} = \frac{(z_{J/\psi} - z_{\text{PV}}^{\text{next}}) \times M_{J/\psi}}{p_z}, \quad (3)$$

where $z_{\text{PV}}^{\text{next}}$ is the position along the z -axis of the primary vertex of the next event. The primary vertex reconstruction efficiency is assumed to be equal for prompt J/ψ and J/ψ from b . Given the high primary vertex reconstruction efficiency, 99.4%, the uncertainty related to this assumption is neglected.

The function describing the t_z distribution of the signal is therefore

$$f_{\text{signal}}(t_z; f_p, f_b, \tau_b) = f_p \delta(t_z) + f_b \frac{e^{-\frac{t_z}{\tau_b}}}{\tau_b} + (1 - f_b - f_p) h_{\text{tail}}(t_z), \quad (4)$$

where f_p is the fraction of prompt J/ψ for which the primary vertex is correctly associated, f_b the fraction of J/ψ from b for which the primary vertex is correctly associated, τ_b the b -hadron pseudo-lifetime and $h_{\text{tail}}(t_z)$ the probability density function taken as the histogram shape obtained from the ‘‘next event’’ method and displayed in Fig. 1 (right). The overall fraction of J/ψ from b is defined as $F_b = \frac{f_b}{f_p + f_b}$. This assumes that the fraction of J/ψ from b in the tail events is equal to the fraction measured with the events for which the primary vertex is correctly reconstructed.

The prompt and b components of the signal function are convolved with a double-Gaussian resolution function

$$f_{\text{resolution}}(t_z; \mu, S_1, S_2, \beta) = \frac{\beta}{\sqrt{2\pi}S_1\sigma} e^{-\frac{(t_z-\mu)^2}{2S_1^2\sigma^2}} + \frac{1-\beta}{\sqrt{2\pi}S_2\sigma} e^{-\frac{(t_z-\mu)^2}{2S_2^2\sigma^2}}. \quad (5)$$

The widths of the Gaussians are equal to the event-by-event t_z measurement errors σ , multiplied by overall scale factors S_1 and S_2 to take into account possible mis-calibration effects on σ . The parameter μ is the bias of the t_z measurement and β the fraction of the Gaussian with the smaller scale factor. For bins with low statistics, a single-Gaussian resolution function is used.

The background consists of random combinations of muons from semi-leptonic b and c decays, which tend to produce positive t_z values, as well as of mis-reconstructed tracks from decays in flight of kaons and pions which contribute both to positive and negative t_z values. The background distribution is parameterised with an empirical function based on the shape of the t_z distribution seen in the J/ψ mass sidebands. It is taken as the sum of a delta function and five exponential components (three for positive t_z and two for negative t_z , the negative and positive exponentials with the largest lifetimes having their lifetimes τ_L fixed to the same value), convolved with the sum of two Gaussian functions of widths σ_1 and σ_2 and fractions β' and $(1 - \beta')$

$$f_{\text{background}}(t_z) = \left[(1 - f_1 - f_2 - f_3 - f_4) \delta(t_z) + \theta(t_z) \left(f_1 \frac{e^{-\frac{t_z}{\tau_1}}}{\tau_1} + f_2 \frac{e^{-\frac{t_z}{\tau_2}}}{\tau_2} \right) + \theta(-t_z) f_3 \frac{e^{\frac{t_z}{\tau_3}}}{\tau_3} + f_4 \frac{e^{-\frac{|t_z|}{\tau_L}}}{2\tau_L} \right] \otimes \left(\frac{\beta'}{\sqrt{2\pi}\sigma_1} e^{-\frac{t_z^2}{2\sigma_1^2}} + \frac{1-\beta'}{\sqrt{2\pi}\sigma_2} e^{-\frac{t_z^2}{2\sigma_2^2}} \right), \quad (6)$$

where $\theta(t_z)$ is the step function. All parameters of the background function are determined independently in each bin of p_T and y , but for bins with low statistics the number of exponential components is reduced. The parameters are obtained from a fit to the t_z distribution of the J/ψ mass sidebands defined as $M_{\mu\mu} \in [2.95; 3.00] \cup [3.20; 3.25] \text{ GeV}/c^2$, and are fixed for the final fit.

The function used to describe the t_z distribution in the final fit is therefore

$$f(t_z; f_p, f_b, f_{J/\psi}, \mu, S_1, S_2, \beta, \tau_b) = f_{J/\psi} \left[\left(f_p \delta(t_z) + f_b \frac{e^{-\frac{t_z}{\tau_b}}}{\tau_b} \right) \otimes f_{\text{resolution}}(t_z; \mu, S_1, S_2, \beta) + (1 - f_b - f_p) h_{\text{tail}}(t_z) \right] + (1 - f_{J/\psi}) f_{\text{background}}(t_z). \quad (7)$$

The total fit function is the sum of the products of the mass and t_z fit functions for the signal and background. Four bins of p_T and y , which contain less than 150 signal J/ψ events as determined from the mass fit, are excluded from the analysis.

As an example, Fig. 1 (right) represents the t_z distribution for one specific bin ($3 < p_T < 4 \text{ GeV}/c$, $2.5 < y < 3.0$) with the fit result superimposed. The RMS of the t_z resolution function is 53 fs and the fraction of tail events to the number of J/ψ signal is $(0.40 \pm 0.01)\%$. As a measure of the fit quality, a χ^2 is calculated for the fit function using a binned event distribution. The resulting fit probability for the histogram of Fig. 1 (right) is equal to 87% and similar good fits are seen for the other bins.

4.2 Luminosity

The luminosity was measured at specific periods during the data taking using both Van der Meer scans [21] and a beam-profile method [22]. Two Van der Meer scans were performed in a single fill. The analysis of these scans yields consistent results for the absolute luminosity scale with a precision of 10%, dominated by the uncertainty in the knowledge of the LHC proton beam currents. In the second approach, six separate periods of stable running were chosen, and the beam-profiles measured using beam-gas and beam-beam interactions. Using these results, correcting for crossing angle effects, and knowing the beam currents, the luminosity in each period is determined following the analysis procedure described in Ref. [23]. Consistent results are found for the absolute luminosity scale in each period, with a precision of 10%, also dominated by the beam current uncertainty. These results are in good agreement with those of the Van der Meer analysis. The knowledge of the absolute luminosity scale is used to calibrate the number of VELO tracks, which is found to be stable throughout the data-taking period and can therefore be used to monitor the instantaneous luminosity of the entire data sample. The integrated luminosity of the runs considered in this analysis is determined to be $5.2 \pm 0.5 \text{ pb}^{-1}$.

4.3 Efficiency calculation

A simulated sample of inclusive, unpolarised J/ψ mesons is used to estimate the total efficiency ϵ_{tot} in each bin of p_T and y . The total efficiency is the product of the geometrical acceptance, the detection, reconstruction and selection efficiencies, and the trigger efficiency. It is displayed in Fig. 2, including both prompt J/ψ and J/ψ from b . The efficiencies are assumed to be equal for prompt J/ψ and J/ψ from b in a given (p_T, y) bin because neither the trigger nor the selection

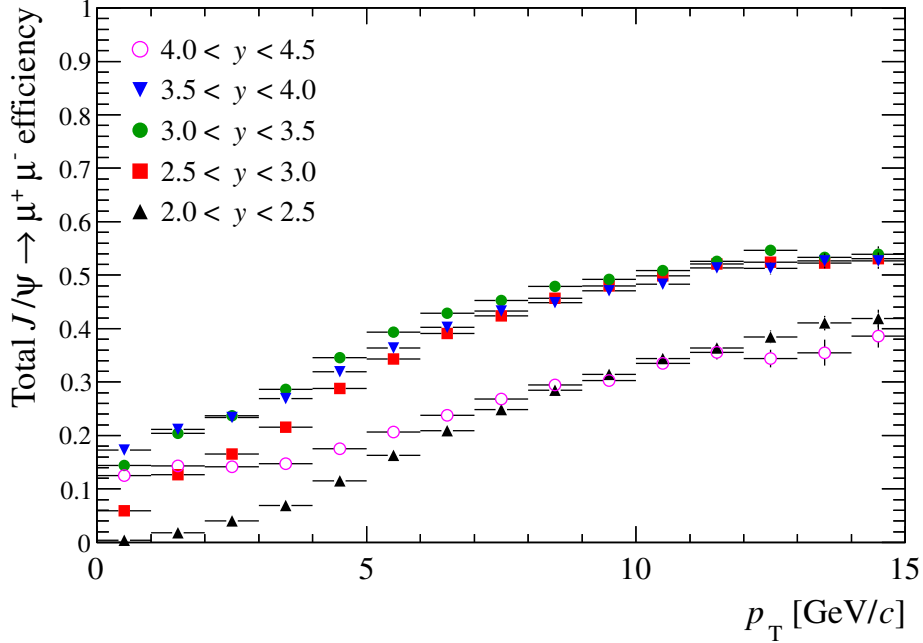


Figure 2: Total J/ψ efficiency, as a function of p_T in bins of y assuming that J/ψ are produced unpolarised. The efficiency is seen to drop somewhat at the edges of the acceptance.

makes use of impact parameter or decay length information. This assumption is confirmed with studies based on simulation.

A correction to the efficiency is applied to take into account the effect of the global event cuts described in Sec. 2, introduced during data taking to remove high multiplicity events. The effect of such cuts on events containing a J/ψ candidate is not well described by the Monte Carlo simulation; it is therefore evaluated from data by using an independent trigger, which accepts events having at least one track reconstructed in either the VELO or the tracking stations. By comparing the number of such triggered signal J/ψ candidates before and after GEC, an efficiency of $(93 \pm 2)\%$ is determined from data.

4.4 Effect of the J/ψ polarisation on the efficiency

The efficiency is evaluated from a Monte Carlo simulation in which the J/ψ is produced unpolarised. However, studies show that non-zero J/ψ polarisation may lead to very different total efficiencies. In this analysis, the efficiency variation is studied in the helicity frame [24].

The angular distribution of the μ^+ from the J/ψ decay is

$$\frac{d^2N}{d\cos\theta d\phi} \propto 1 + \lambda_\theta \cos^2\theta + \lambda_{\theta\phi} \sin 2\theta \cos\phi + \lambda_\phi \sin^2\theta \cos 2\phi, \quad (8)$$

where θ is defined as the angle between the direction of the μ^+ momentum in the J/ψ centre-of-mass frame and the direction of the J/ψ momentum in the centre-of-mass frame of the colliding protons, and ϕ is the azimuthal angle measured with respect to the production plane formed by the momenta of the colliding protons in the J/ψ rest frame. When $\lambda_\phi = 0$ and $\lambda_{\theta\phi} = 0$, the values $\lambda_\theta = +1, -1, 0$ correspond to fully transverse, fully longitudinal, and no polarisation, respectively, which are the three default polarisation scenarios considered in this analysis.

The polarisation significantly affects the acceptance and reconstruction efficiencies. The relative efficiency change for prompt J/ψ varies between 3% and 30% depending on p_T and y , when comparing to the unpolarised case. Therefore, the measurement of the differential prompt J/ψ cross-section will be given for the three default polarisations and a separate uncertainty due to the polarisation will be assigned to the integrated cross-section.

Three other polarisation configurations were studied, corresponding to $(\lambda_\theta, \lambda_\phi, \lambda_{\theta\phi}) = (+1, 0, -1)$, $(0, 1/\sqrt{2}, -1/2)$ and $(0, -1/\sqrt{2}, -1/2)$; these do not produce variations of the measured prompt cross-sections larger than those obtained with the default $(\pm 1, 0, 0)$ scenarios, except in some of the bins with $4 < y < 4.5$ where the variations are up to 25% larger.

The Monte Carlo simulation includes polarisation of J/ψ from b as measured at BABAR for B^0 and B^+ decays [25]. The simulation shows that the polarisation that the J/ψ acquires in b decays is largely diluted when using as helicity quantisation axis the J/ψ momentum in the laboratory frame instead of the J/ψ momentum in the b -hadron rest frame, which is the natural polarisation axis. The effect of the J/ψ from b polarisation on the J/ψ acceptance and reconstruction efficiencies is less than 0.5%; therefore, no systematic uncertainty is assigned to the J/ψ from b cross-section measurement from the unknown J/ψ polarisation.

5 Systematic uncertainties

The different contributions to the systematic uncertainties affecting the cross-section measurement are discussed in the following and summarised in Table 1.

Due to the finite p_T and y resolutions, J/ψ candidates can be assigned to a wrong p_T bin (inter-bin cross-feed in Table 1). According to Monte Carlo simulations, the average p_T resolution is $12.7 \pm 0.2 \text{ MeV}/c$ and the y resolution is $(1.4 \pm 0.1) \times 10^{-3}$. The effect of the y resolution is negligible compared to the bin width of $\Delta y = 0.5$. The effect of the p_T resolution is estimated by recomputing the efficiency tables after smearing the p_T values with a Gaussian distribution of $\sigma = 20 \text{ MeV}/c$. The maximum relative deviation observed is 0.5% and this is the value used as systematic uncertainty for the differential cross-section measurement. The effect on the total cross-section is much smaller and is ignored.

The influence of the choice of the fit function used to describe the shape of the dimuon mass distribution is estimated by fitting the J/ψ invariant mass distribution with the sum of two Crystal Ball functions. The relative difference of 1% in the number of signal events is taken as systematic uncertainty.

A fraction of J/ψ events have a lower mass because of the radiative tail. Based on Monte Carlo studies, 2% of the J/ψ signal is estimated to be outside the analysis mass window ($M_{\mu\mu} < 2.95 \text{ GeV}/c^2$) and not counted as signal. The fitted signal yields are therefore corrected by 2%, and an uncertainty of 1% is assigned to the cross-section measurements.

To cross-check and assign a systematic uncertainty to the Monte Carlo determination of the muon identification efficiency, the single track muon identification efficiency is measured on data using a tag-and-probe method. This method reconstructs J/ψ candidates in which one muon is identified by the muon system (“tag”) and the other one (“probe”) is identified selecting a track depositing the energy of minimum-ionising particles in the calorimeters. The absolute muon identification efficiency is then evaluated on the probe muon, as a function of the muon momentum. The ratio of the muon identification efficiency measured in data to that obtained in the Monte Carlo simulation is convolved with the momentum distribution of muons from J/ψ to compute a correction factor to apply on simulation-based efficiencies. This factor is found to

Table 1: Summary of systematic uncertainties.

Source	Systematic uncertainty (%)
<i>Correlated between bins</i>	
Inter-bin cross-feed	0.5
Mass fits	1.0
Radiative tail	1.0
Muon identification	1.1
Tracking efficiency	8.0
Track χ^2	1.0
Vertexing	0.8
GEC	2.0
$\mathcal{B}(J/\psi \rightarrow \mu^+ \mu^-)$	1.0
Luminosity	10.0
<i>Uncorrelated between bins</i>	
Bin size	0.1 to 15.0
Trigger	1.7 to 4.5
<i>Applied only to J/ψ from b cross-sections, correlated between bins</i>	
GEC efficiency on B events	2.0
t_z fits	3.6
<i>Applied only to the extrapolation of the $b\bar{b}$ cross-section</i>	
b hadronisation fractions	2.0
$\mathcal{B}(b \rightarrow J/\psi X)$	9.0

be 1.024 ± 0.011 and is consistent with being constant over the full J/ψ transverse momentum and rapidity range; the error on the correction factor is used as a systematic uncertainty. The residual misalignment between the tracking system and the muon detectors is accounted for in this systematic uncertainty.

Tracking studies have shown that the Monte Carlo simulation reproduces the track-finding efficiency in data within 4%. A systematic uncertainty of 4% for each muon is therefore assigned, resulting in a total systematic uncertainty of 8% due to the knowledge of the track reconstruction efficiency [26]. The effects of the residual misalignment of the tracking system are included in this systematic uncertainty.

The selection includes a requirement on the track fit quality, which may not be reliably simulated. A systematic uncertainty of 0.5% is assigned per track, which is the relative difference between the efficiency of this requirement in the simulation and data.

Similarly, for the cut on the J/ψ vertex χ^2 probability, a difference of 1.6% is measured between the cut efficiency computed in data and simulation. The Monte Carlo efficiency is corrected for this difference and a systematic uncertainty of 0.8% (half of the correction) is

assigned.

The unknown J/ψ transverse momentum and rapidity spectra inside the bins affect the efficiency values used to extract the cross-section, because an average value of the efficiency is computed in each bin. This effect is important close to the edges of the fiducial region. To take into account possible efficiency variations inside the bins, each bin is divided into four sub-bins (two bins in p_T and two bins in y) and the relative deviation between the bin efficiency and the average of the efficiencies in the sub-bins is taken as a systematic uncertainty.

The trigger efficiency can be determined using a trigger-unbiased sample of events that would still be triggered if the J/ψ candidate were removed. The efficiency obtained with this method in each (p_T, y) bin is used to check the efficiencies measured in the simulation. The systematic uncertainty associated with the trigger efficiency is the difference between the trigger efficiency measured in the data and in the simulation. The largest uncertainties are obtained for the high rapidity bins.

The statistical error on the GEC efficiency (2%) is taken as an additional systematic uncertainty associated with the trigger. This efficiency is extracted from data as explained in Sec. 4.3; it is essentially the efficiency of the GEC on prompt J/ψ . In the simulation, a 2% difference is seen between the prompt J/ψ and the J/ψ from b efficiency, which is used as an additional systematic uncertainty, applied only to the J/ψ from b cross-section measurement.

Uncertainties related to the t_z fit procedure are taken into account by varying the central value of the prompt J/ψ component, μ , which is found to be different from zero. This shift could be due to an improper description of the background for events close to $t_z = 0$. The impact of such a shift is studied by fixing μ at two extreme values, $\mu = -3$ fs and $\mu = 3$ fs and repeating the t_z fit. The relative variation of the number of J/ψ from b , 3.6%, is used as a systematic uncertainty.

The extrapolation to the full polar angle to obtain the $b\bar{b}$ cross-section uses the average branching fraction of inclusive b -hadron decays to J/ψ measured at LEP, i.e., $\mathcal{B}(b \rightarrow J/\psi X) = (1.16 \pm 0.10)\%$ [27]. The underlying assumption is that the b -hadron fractions in pp collisions at $\sqrt{s} = 7$ TeV are identical to those seen in $Z \rightarrow b\bar{b}$ decays. However, the b hadronisation fractions may differ at hadronic machines. To estimate the systematic uncertainty due to possibly different fractions, the $\mathcal{B}(b \rightarrow J/\psi X)$ is computed by taking as input for the calculation the fractions measured at the Tevatron [28, 29] and assuming the partial widths of B_u, B_d, B_s and Λ_b to $J/\psi X$ to be equal. The relative difference between the estimates of the branching fractions based on the fragmentation functions measured at LEP and at the Tevatron, 2%, is taken as systematic uncertainty, which only affects the extrapolation of the $b\bar{b}$ cross-section.

6 Results

The measured double-differential cross-sections for prompt J/ψ and J/ψ from b in the various (p_T, y) bins, after all corrections and assuming no polarisation, are given in Tables 4 and 5, and displayed in Figs. 3 and 4. The results for full transverse and full longitudinal polarisation of the J/ψ in the helicity frame are given in Tables 6 and 7, and displayed in Fig. 5.

The integrated cross-section for prompt J/ψ production in the defined fiducial region, summing over all bins of the analysis, is

$$\sigma(\text{prompt } J/\psi, p_T < 14 \text{ GeV}/c, 2.0 < y < 4.5) = 10.52 \pm 0.04 \pm 1.40_{-2.20}^{+1.64} \mu\text{b}, \quad (9)$$

where the first uncertainty is statistical and the second systematic. The result is quoted assuming

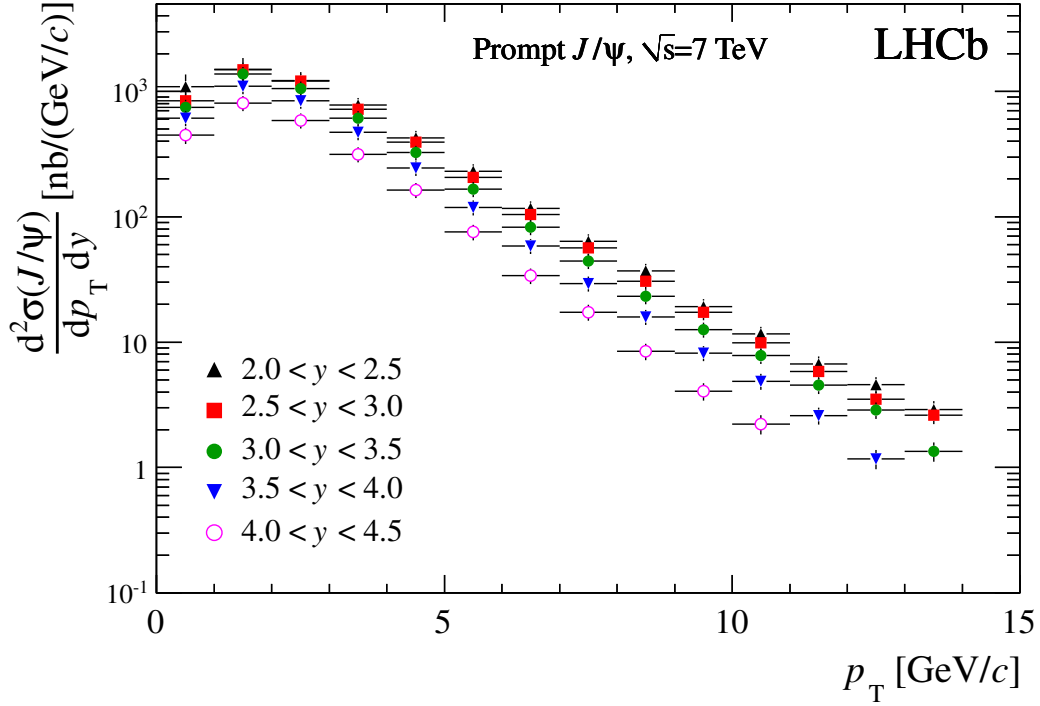


Figure 3: Differential production cross-section for prompt J/ψ as a function of p_T in bins of y , assuming that prompt J/ψ are produced unpolarised. The errors are the quadratic sums of the statistical and systematic uncertainties.

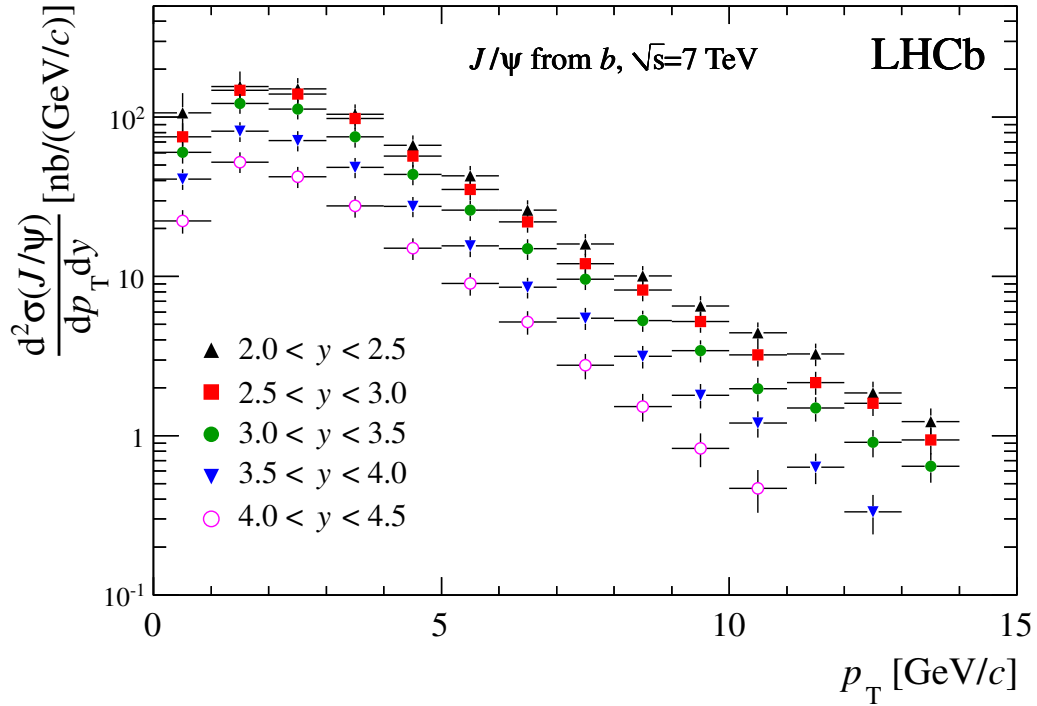


Figure 4: Differential production cross-section for J/ψ from b as a function of p_T in bins of y . The errors are the quadratic sums of the statistical and systematic uncertainties.

Table 2: Mean p_T and RMS for prompt J/ψ (assumed unpolarised) and J/ψ from b . The first uncertainty is statistical, the second systematic and the third for prompt J/ψ the uncertainty due to the unknown polarisation.

p_T range		Prompt J/ψ		J/ψ from b	
(GeV/c)	y bin	$\langle p_T \rangle$ (GeV/c)	RMS p_T (GeV/c)	$\langle p_T \rangle$ (GeV/c)	RMS p_T (GeV/c)
0–14	2.0–2.5	$2.51 \pm 0.03 \pm 0.10^{+0.02}_{-0.01}$	$1.80 \pm 0.01 \pm 0.04^{+0.00}_{-0.02}$	$3.06 \pm 0.09 \pm 0.11$	$2.22 \pm 0.02 \pm 0.04$
0–14	2.5–3.0	$2.53 \pm 0.01 \pm 0.06^{+0.06}_{-0.04}$	$1.74 \pm 0.01 \pm 0.01^{+0.02}_{-0.02}$	$3.04 \pm 0.02 \pm 0.05$	$2.12 \pm 0.01 \pm 0.01$
0–14	3.0–3.5	$2.46 \pm 0.01 \pm 0.02^{+0.07}_{-0.05}$	$1.68 \pm 0.01 \pm 0.01^{+0.02}_{-0.01}$	$2.93 \pm 0.02 \pm 0.02$	$2.03 \pm 0.01 \pm 0.01$
0–13	3.5–4.0	$2.38 \pm 0.01 \pm 0.02^{+0.07}_{-0.05}$	$1.61 \pm 0.01 \pm 0.01^{+0.01}_{-0.01}$	$2.82 \pm 0.02 \pm 0.02$	$1.92 \pm 0.02 \pm 0.01$
0–11	4.0–4.5	$2.29 \pm 0.01 \pm 0.02^{+0.08}_{-0.05}$	$1.50 \pm 0.01 \pm 0.01^{+0.01}_{-0.01}$	$2.73 \pm 0.03 \pm 0.03$	$1.77 \pm 0.03 \pm 0.01$

unpolarised J/ψ and the last error indicates the uncertainty related to this assumption. The integrated cross-section for the production of J/ψ from b in the same fiducial region is

$$\sigma(J/\psi \text{ from } b, p_T < 14 \text{ GeV}/c, 2.0 < y < 4.5) = 1.14 \pm 0.01 \pm 0.16 \mu\text{b}, \quad (10)$$

where the first uncertainty is statistical and the second systematic.

The mean and RMS of the p_T spectrum in each y bin are displayed in Table 2. The J/ψ mesons from b -hadron decays have a mean p_T and RMS which are approximately 20% larger than those of prompt J/ψ mesons. For each J/ψ source, the mean p_T and RMS are observed to decrease with increasing y .

Table 3 and Fig. 6 show the differential cross-sections $\frac{d\sigma}{dy}$ integrated over p_T , both for unpolarised prompt J/ψ and J/ψ from b . For the two production sources, the cross-sections decrease significantly between the central and forward regions of the LHCb acceptance.

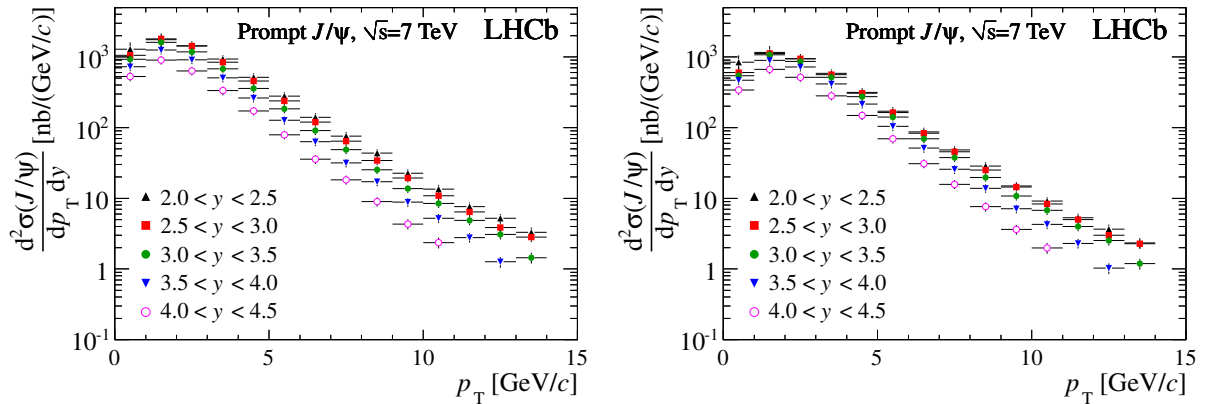


Figure 5: Differential production cross-section for prompt J/ψ as a function of p_T in bins of y , assuming full transverse (*left*) or full longitudinal (*right*) J/ψ polarisation. The errors are the quadratic sums of the statistical and systematic uncertainties.

Table 3: $\frac{d\sigma}{dy}$ in nb for prompt J/ψ (assumed unpolarised) and J/ψ from b , integrated over p_T . The first uncertainty is statistical, the second is the component of the systematic uncertainty that is uncorrelated between bins and the third is the correlated component.

p_T range (GeV/c)	y bin	Prompt J/ψ	J/ψ from b
0 – 14	2.0 – 2.5	$5504 \pm 83 \pm 381 \pm 726$	$697 \pm 27 \pm 40 \pm 96$
0 – 14	2.5 – 3.0	$5096 \pm 21 \pm 142 \pm 672$	$608 \pm 7 \pm 13 \pm 84$
0 – 14	3.0 – 3.5	$4460 \pm 14 \pm 59 \pm 589$	$479 \pm 5 \pm 5 \pm 66$
0 – 13	3.5 – 4.0	$3508 \pm 12 \pm 40 \pm 463$	$307 \pm 4 \pm 3 \pm 42$
0 – 11	4.0 – 4.5	$2462 \pm 12 \pm 48 \pm 325$	$180 \pm 4 \pm 3 \pm 25$

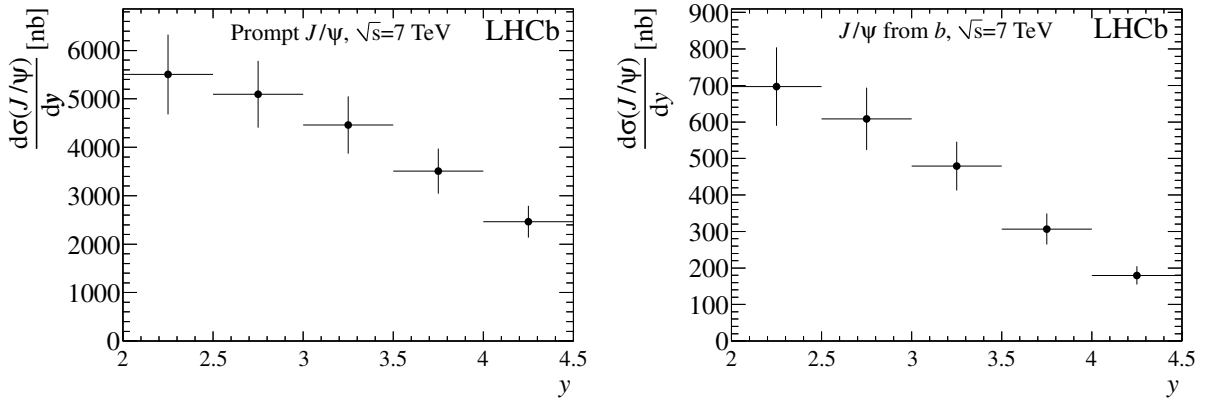


Figure 6: Differential production cross-section as a function of y integrated over p_T , for unpolarised prompt J/ψ (left) and J/ψ from b (right). The errors are the quadratic sums of the statistical and systematic uncertainties.

6.1 Fraction of J/ψ from b

Table 8 and Fig. 7 give the values of the fraction of J/ψ from b in the different bins assuming that the prompt J/ψ are produced unpolarised. The third uncertainty in Table 8 gives the deviation from the central value when the prompt J/ψ are fully transversely or fully longitudinally polarised in the helicity frame.

In Fig. 7, only the statistical and systematic uncertainties are displayed, added quadratically, but not the uncertainties associated with the prompt J/ψ polarisation. The fraction of J/ψ from b increases as a function of p_T . For a constant p_T , the fraction of J/ψ from b decreases with increasing y , indicating that b -hadrons are produced more centrally than prompt J/ψ .

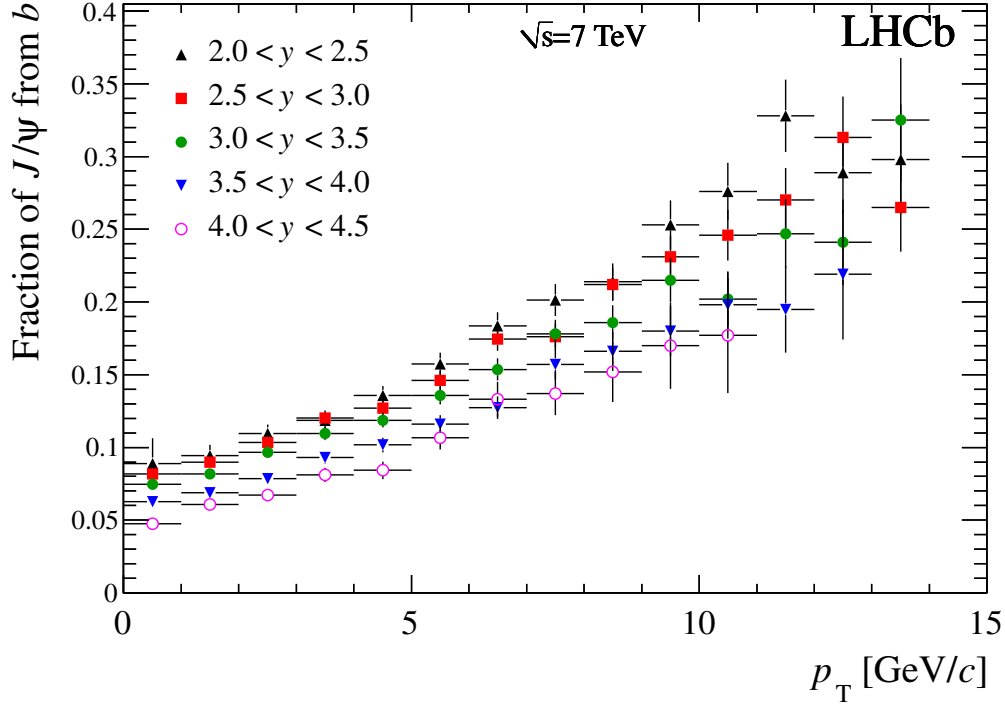


Figure 7: Fraction of J/ψ from b as a function of p_T , in bins of y .

6.2 Cross-section extrapolation

Using the LHCb Monte Carlo simulation based on PYTHIA 6.4 [14] and EvtGen [16], the result quoted in Eq. (10) is extrapolated to the full polar angle range

$$\sigma(pp \rightarrow b\bar{b}X) = \alpha_{4\pi} \frac{\sigma(J/\psi \text{ from } b, p_T < 14 \text{ GeV}/c, 2.0 < y < 4.5)}{2 \mathcal{B}(b \rightarrow J/\psi X)}, \quad (11)$$

where $\alpha_{4\pi} = 5.88$ is the ratio of J/ψ from b events in the full range to the number of events in the region $2.0 < y < 4.5$ and $\mathcal{B}(b \rightarrow J/\psi X) = (1.16 \pm 0.10)\%$ is the average branching fraction of inclusive b -hadron decays to J/ψ measured at LEP [27]. The result is

$$\sigma(pp \rightarrow b\bar{b}X) = 288 \pm 4 \pm 48 \mu\text{b}, \quad (12)$$

where the first uncertainty is statistical and the second systematic. The systematic uncertainty includes the uncertainties on the b fractions (2%) and on $\mathcal{B}(b \rightarrow J/\psi X)$. No additional uncertainty has been included for the extrapolation factor $\alpha_{4\pi}$ estimated from the simulation. The above result is in excellent agreement with $\sigma(pp \rightarrow b\bar{b}X) = 284 \pm 20 \pm 49 \mu\text{b}$ obtained from b decays into $D^0 \mu \nu X$ [26]. The extrapolation factor $\alpha_{4\pi}$ has also been estimated using predictions made in the framework of fixed-order next-to-leading log (FONLL) computations [30], and found to be equal to $\alpha_{4\pi}^{\text{FONLL}} = 5.21$.

7 Comparison with theoretical models

Figure 8 compares the LHCb measurement of the differential prompt J/ψ production with several recent theory predictions in the LHCb acceptance region:

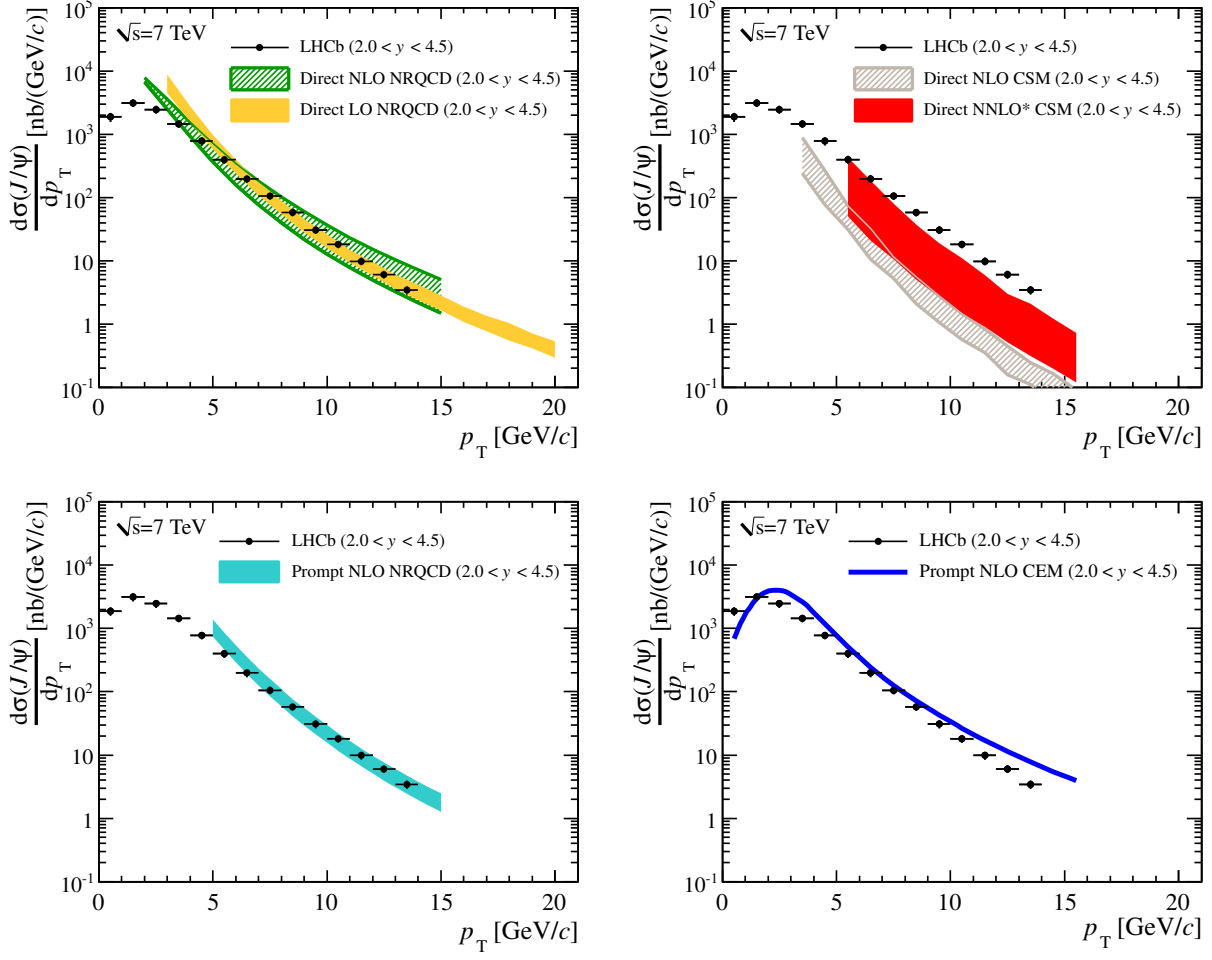


Figure 8: Comparison of the LHCb results for the differential prompt J/ψ production for unpolarised J/ψ (circles with error bars) with: (top, left) direct J/ψ production as predicted by LO and NLO NRQCD; (top, right) direct J/ψ production as predicted by NLO and NNLO \star CSM; (bottom, left) prompt J/ψ production as predicted by NLO NRQCD; (bottom, right) prompt J/ψ production as predicted by NLO CEM. A more detailed description of the models and their references is given in the text.

- top, left: direct J/ψ production as calculated from NRQCD at leading-order in α_s (LO, filled orange uncertainty band) [31] and next-to-leading order (NLO), with colour-octet long distance matrix elements determined from HERA and Tevatron data (hatched green uncertainty band) [32], summing the colour-singlet and colour-octet contributions.
- top, right: direct production as calculated from a NNLO \star colour-singlet model (CSM, filled red uncertainty band) [11, 33]. The notation NNLO \star denotes an evaluation that is not a complete next-to-next leading order computation and that can be affected by logarithmic corrections, which are however not easily quantifiable. Direct production as calculated from NLO CSM (hatched grey uncertainty band) [7, 9] is also represented.
- bottom, left: prompt J/ψ production as calculated from NRQCD at NLO, including contributions from χ_c and $\psi(2S)$ decays, summing the colour-singlet and colour-octet contributions [34].

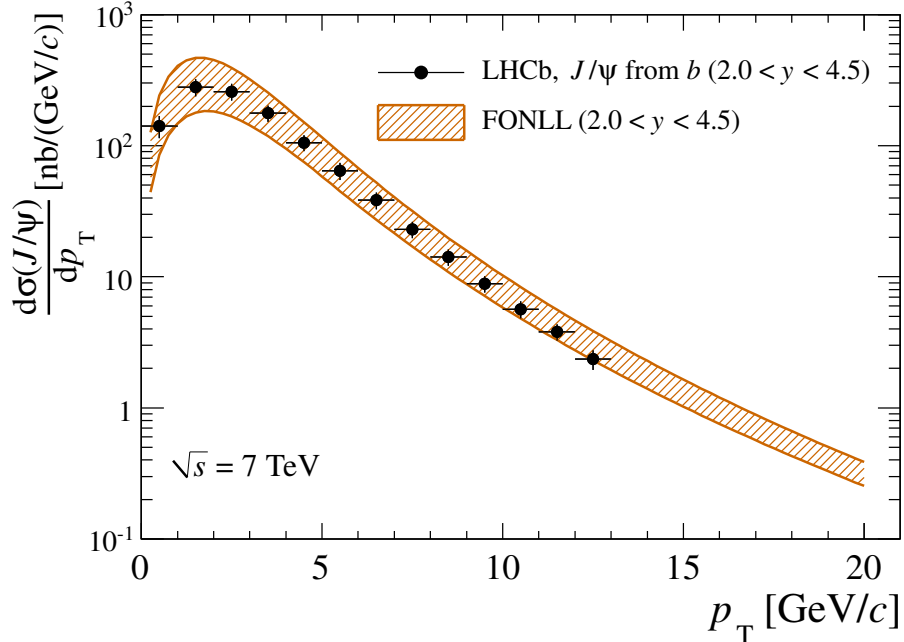


Figure 9: Comparison of the LHCb results for the differential J/ψ from b production for unpolarised J/ψ (circles with error bars) with J/ψ from b production as predicted by FONLL (hatched orange uncertainty band). A more detailed description of the model and its references is given in the text.

- bottom, right: prompt J/ψ production as calculated from a NLO colour-evaporation model (CEM), including contributions from χ_c and $\psi(2S)$ decays [35].

It should be noted that some of the theoretical models compute the direct J/ψ production, whereas the prompt J/ψ measurement includes J/ψ from χ_c decays and, to a smaller extent, $\psi(2S)$ decays. However, if one takes into account the feed-down contribution, which has been estimated to be of the order of 30% averaging over several experimental measurements at lower energies [36], a satisfactory agreement is found with the theoretical predictions.

Figure 9 shows a comparison of the LHCb measurement of the differential J/ψ from b cross-section with a calculation based on the FONLL formalism [30]. This model predicts the b -quark production cross-section, and includes the fragmentation of the b -quark into b -hadrons and their decay into J/ψ mesons. The measurements show a very good agreement with the calculation.

8 Conclusions

The differential cross-section for J/ψ production is measured as a function of the J/ψ transverse momentum and rapidity in the forward region, $2.0 < y < 4.5$. The analysis is based on a data sample corresponding to an integrated luminosity of 5.2 pb^{-1} collected at the Large Hadron Collider at a centre-of-mass energy of $\sqrt{s} = 7 \text{ TeV}$, and the contributions of prompt J/ψ and J/ψ from b production are individually measured. The results obtained are in good agreement with earlier measurements of the J/ψ production cross-section in pp collisions at the same centre-of-mass energy, performed by CMS in a region corresponding to the low rapidity part of the LHCb acceptance [12]. This measurement is the first measurement of prompt J/ψ and J/ψ from b production in the forward region at $\sqrt{s} = 7 \text{ TeV}$.

A comparison with recent theoretical models shows good general agreement with the measured prompt J/ψ cross-section in the LHCb acceptance at high p_T . This confirms the progress in the theoretical calculations of J/ψ hadroproduction, even if the uncertainties on the predictions are still large. However, the measurement of the differential cross-section alone is not sufficient to be able to discriminate amongst the various models, and studies of other observables such as the J/ψ polarisation will be necessary. The measurement of the cross-section for J/ψ from b is found to agree very well with FONLL predictions. An estimate of the $b\bar{b}$ cross-section in pp collisions at $\sqrt{s} = 7\text{TeV}$ is also obtained, which is in excellent agreement with measurements performed analysing different b decay modes [26].

Acknowledgments

We express our gratitude to our colleagues in the CERN accelerator departments for the excellent performance of the LHC. We thank the technical and administrative staff at CERN and at the LHCb institutes, and acknowledge support from the National Agencies: CAPES, CNPq, FAPERJ and FINEP (Brazil); CERN; NSFC (China); CNRS/IN2P3 (France); BMBF, DFG, HGF and MPG (Germany); SFI (Ireland); INFN (Italy); FOM and NWO (Netherlands); SCSR (Poland); ANCS (Romania); MinES of Russia and Rosatom (Russia); MICINN, XUNGAL and GENCAT (Spain); SNSF and SER (Switzerland); NAS Ukraine (Ukraine); STFC (United Kingdom); NSF (USA). We also acknowledge the support received from the ERC under FP7 and the Region Auvergne.

We thank P. Artoisenet, M. Butenschön, M. Cacciari, K. T. Chao, B. Kniehl, J.-P. Lansberg and R. Vogt for providing theoretical predictions of J/ψ cross-sections in the LHCb acceptance range.

References

- [1] N. Brambilla *et al.*, “Heavy quarkonium: progress, puzzles, and opportunities”, *Eur. Phys. J. C* **71** (2011) 1534, [arXiv:1010.5827 \[hep-ph\]](#).
- [2] C.-H. Chang, “Hadronic production of J/ψ associated with a gluon”, *Nucl. Phys. B* **172** (1980) 425; R. Baier and R. Rückl, “Hadronic collisions: a quarkonium factory”, *Z. Phys. C* **19** (1983) 251.
- [3] The CDF Collaboration, F. Abe *et al.*, “ J/ψ and $\psi(2S)$ production in $p\bar{p}$ collisions at $\sqrt{s} = 1.8\text{TeV}$ ”, *Phys. Rev. Lett.* **79** (1997) 572; The CDF Collaboration, F. Abe *et al.*, “Production of J/ψ mesons from χ_c meson decays in $p\bar{p}$ collisions at $\sqrt{s} = 1.8\text{TeV}$ ”, *Phys. Rev. Lett.* **79** (1997) 578.
- [4] M. Cacciari and M. Greco, “ J/ψ production via fragmentation at the Tevatron”, *Phys. Rev. Lett.* **73** (1994) 1586, [arXiv:hep-ph/9405241](#); E. Braaten, M. A. Doncheski, S. Fleming and M. L. Mangano, “Fragmentation production of J/ψ and ψ' at the Tevatron”, *Phys. Lett. B* **333** (1994) 548, [arXiv:hep-ph/9405407](#).
- [5] G. T. Bodwin, E. Braaten and G. P. Lepage, “Rigorous QCD analysis of inclusive annihilation and production of heavy quarkonium”, *Phys. Rev. D* **51** (1995) 1125, erratum *ibid. D* **55** (1997) 5853, [arXiv:hep-ph/9407339](#); P. L. Cho and A. K. Leibovich, “Color octet quarkonia production”, *Phys. Rev. D* **53** (1996) 150, [arXiv:hep-ph/9505329](#); P. L. Cho

- and A. K. Leibovich, “Color octet quarkonia production II”, Phys. Rev. D **53** (1996) 6203, [arXiv:hep-ph/9511315](#).
- [6] The CDF Collaboration, A. Abulencia *et al.*, “Polarization of J/ψ and $\psi(2S)$ mesons produced in $p\bar{p}$ collisions at $\sqrt{s} = 1.96\text{TeV}$ ”, Phys. Rev. Lett. **99** (2007) 132001, [arXiv:0704.0638 \[hep-ex\]](#).
- [7] P. Artoisenet, J.-P. Lansberg and F. Maltoni, “Hadroproduction of J/ψ and Υ in association with a heavy-quark pair”, Phys. Lett. B **653** (2007) 60, [arXiv:hep-ph/0703129](#).
- [8] S. P. Baranov, “Topics in associated $J/\psi + c + \bar{c}$ production at modern colliders”, Phys. Rev. D **73** (2006) 074021.
- [9] J. M. Campbell, F. Maltoni and F. Tramontano, “QCD corrections to J/ψ and Υ production at hadron colliders”, Phys. Rev. Lett. **98** (2007) 252002, [arXiv:hep-ph/0703113](#).
- [10] P. Artoisenet, “QCD corrections to heavy quarkonium production”, AIP Conf. Proc. **1038** (2008) 55.
- [11] P. Artoisenet, J. M. Campbell, J.-P. Lansberg, F. Maltoni and F. Tramontano, “ Υ production at Fermilab Tevatron and LHC energies”, Phys. Rev. Lett. **101** (2008) 152001, [arXiv:0806.3282 \[hep-ph\]](#).
- [12] The CMS Collaboration, V. Khachatryan *et al.*, “Prompt and non-prompt J/ψ production in pp collisions at $\sqrt{s} = 7\text{TeV}$ ”, Eur. Phys. J. C **71** (2011) 1575, [arXiv:1011.4193 \[hep-ex\]](#).
- [13] The LHCb Collaboration, A. A. Alves *et al.*, “The LHCb detector at the LHC”, JINST **3** (2008) S08005.
- [14] T. Sjöstrand, S. Mrenna and P. Z. Skands, “PYTHIA 6.4 physics and manual”, version 6.422, J. High Energy Phys. **0605** (2006) 026, [arXiv:hep-ph/0603175](#).
- [15] I. Belyaev *et al.*, “Handling of the generation of primary events in Gauss, the LHCb simulation framework”, [CERN-LHCb-PROC-2010-056](#), to appear in the proceedings of NSS 2010, *the 2010 Nuclear Science Symposium, October 30-November 6, 2010, Knoxville, USA*.
- [16] D. J. Lange, “The EvtGen particle decay simulation package”, Nucl. Instrum. Methods A **462** (2001) 152.
- [17] The GEANT4 Collaboration, S. Agostinelli *et al.*, “GEANT4: a simulation toolkit”, version 9.2, Nucl. Instrum. Methods A **506** (2003) 250.
- [18] P. Golonka and Z. Was, “PHOTOS Monte Carlo: a precision tool for QED corrections in Z and W decays”, version 2.15, Eur. Phys. J. C **45** (2006) 97, [arXiv:hep-ph/0506026](#).
- [19] The Particle Data Group, K. Nakamura *et al.*, “Review of particle physics”, J. Phys. G **37** (2010) 075021.
- [20] J. E. Gaiser, “Charmonium spectroscopy from radiative decays of the J/ψ and ψ' ”, Ph.D. Thesis, [SLAC-R-255](#) (1982); T. Skwarnicki, “A study of the radiative cascade transitions between the Υ' and Υ resonances”, Ph.D. Thesis, [DESY-F31-86-02](#) (1986).
- [21] S. van der Meer, “Calibration of the effective beam height in the ISR”, [ISR-PO/68-31](#) (1968).
- [22] M. Ferro-Luzzi, “Proposal for an absolute luminosity determination in colliding beam experiments using vertex detection of beam-gas interactions”, Nucl. Instrum. Methods A **553** (2005) 388.

- [23] The LHCb Collaboration, R. Aaij *et al.*, “Prompt K_S^0 production in pp collisions at $\sqrt{s} = 0.9\text{TeV}$ ”, Phys. Lett. B **693** (2010) 69, [arXiv:1008.3105 \[hep-ex\]](#).
- [24] K. Gottfried and J. D. Jackson, “On the connection between production mechanism and decay of resonances at high-energies”, Nuovo Cimento **33** (1964) 309; C. S. Lam and W.-K. Tung, “A systematic approach to inclusive lepton pair production in hadronic collisions”, Phys. Rev. D **18** (1978) 2447.
- [25] The BABAR Collaboration, B. Aubert *et al.*, “Study of inclusive production of charmonium in B decay”, Phys. Rev. D **67** (2003) 032002, [arXiv:hep-ex/0207097](#).
- [26] The LHCb Collaboration, R. Aaij *et al.*, “Measurement of $\sigma(pp \rightarrow b\bar{b}X)$ at $\sqrt{s} = 7\text{TeV}$ in the forward region”, Phys. Lett. B **694** (2010) 209, [arXiv:1009.2731 \[hep-ex\]](#).
- [27] The DELPHI Collaboration, P. Abreu *et al.*, “ J/ψ production in the hadronic decays of the Z ”, Phys. Lett. B **341** (1994) 109; The L3 Collaboration, O. Adriani *et al.*, “ χ_c production in hadronic Z decays”, Phys. Lett. B **317** (1993) 467; The ALEPH Collaboration, D. Buskulic *et al.*, “Measurements of mean lifetime and branching fractions of b hadrons decaying to J/ψ ”, Phys. Lett. B **295** (1992) 396.
- [28] The CDF Collaboration, T. Aaltonen *et al.*, “Measurement of ratios of fragmentation fractions for bottom hadrons in $p\bar{p}$ collisions at $\sqrt{s} = 1.96\text{TeV}$ ”, Phys. Rev. D **77** (2008) 072003, [arXiv:0801.4375 \[hep-ex\]](#).
- [29] The Heavy Flavour Averaging Group (HFAG), D. Asner *et al.*, “Averages of b -hadron, c -hadron, and τ -lepton properties”, [arXiv:1010.1589 \[hep-ex\]](#).
- [30] M. Cacciari, M. Greco and P. Nason, “The p_T spectrum in heavy-flavour hadroproduction”, J. High Energy Phys. **9805** (1998) 007, [arXiv:hep-ph/9803400](#); M. Cacciari, S. Frixione and P. Nason, “The p_T spectrum in heavy-flavor photoproduction”, J. High Energy Phys. **0103** (2001) 006, [arXiv:hep-ph/0102134](#).
- [31] P. Artoisenet, “Quarkonium production at the Tevatron and the LHC”, PoS **ICHEP 2010** (2010) 192.
- [32] M. Butenschön and B. A. Kniehl, “Reconciling J/ψ production at HERA, RHIC, Tevatron, and LHC with NRQCD factorization at next-to-leading order”, Phys. Rev. Lett. **106** (2011) 022301, [arXiv:1009.5662 \[hep-ph\]](#).
- [33] J.-P. Lansberg, “On the mechanisms of heavy-quarkonium hadroproduction”, Eur. Phys. J. C **61** (2009) 693, [arXiv:0811.4005 \[hep-ph\]](#).
- [34] Y. Q. Ma, K. Wang and K. T. Chao, “ J/ψ (ψ') production at Tevatron and LHC at $O(\alpha_s^4 v^4)$ in nonrelativistic QCD”, Phys. Rev. Lett. **106** (2011) 042002, [arXiv:1009.3655 \[hep-ph\]](#).
- [35] A. D. Frawley, T. Ullrich and R. Vogt, “Heavy flavor in heavy-ion collisions at RHIC and RHIC II”, Phys. Rep. **462** (2008) 125, [arXiv:0806.1013 \[nucl-ex\]](#).
- [36] P. Faccioli *et al.*, “Study of ψ' and χ_c decays as feed-down sources of J/ψ hadroproduction”, J. High Energy Phys. **0810** (2008) 004, [arXiv:0809.2153 \[hep-ph\]](#).

Table 4: $\frac{d^2\sigma}{dp_T dy}$ in nb/(GeV/c) for prompt J/ψ in bins of the J/ψ transverse momentum and rapidity, assuming no polarisation. The first error is statistical, the second is the component of the systematic uncertainty that is uncorrelated between bins and the third is the correlated component.

p_T (GeV/c)	$2.0 < y < 2.5$	$2.5 < y < 3.0$	$3.0 < y < 3.5$
0– 1	1091 ± 70 ± 226 ± 144	844 ± 13 ± 133 ± 111	749 ± 7 ± 46 ± 99
1– 2	1495 ± 38 ± 282 ± 197	1490 ± 12 ± 39 ± 197	1376 ± 8 ± 26 ± 182
2– 3	1225 ± 20 ± 109 ± 162	1214 ± 9 ± 24 ± 160	1053 ± 7 ± 19 ± 139
3– 4	777 ± 11 ± 44 ± 103	719 ± 6 ± 18 ± 95	611 ± 5 ± 14 ± 81
4– 5	424 ± 6 ± 22 ± 56	392 ± 3 ± 12 ± 52	325 ± 3 ± 9 ± 43
5– 6	230 ± 4 ± 12 ± 30	206 ± 2 ± 8 ± 27	167 ± 2 ± 5 ± 22
6– 7	116 ± 2 ± 6 ± 15	104 ± 1 ± 4 ± 14	82 ± 1 ± 3 ± 11
7– 8	64 ± 1 ± 3 ± 8	57 ± 1 ± 3 ± 7	44 ± 1 ± 1 ± 6
8– 9	37 ± 1 ± 1 ± 5	31 ± 1 ± 1 ± 4	23 ± 1 ± 1 ± 3
9–10	19.3 ± 0.7 ± 0.5 ± 2.6	17.4 ± 0.5 ± 0.2 ± 2.3	12.6 ± 0.4 ± 0.1 ± 1.7
10–11	11.6 ± 0.5 ± 0.3 ± 1.5	9.8 ± 0.4 ± 0.1 ± 1.3	7.8 ± 0.3 ± 0.1 ± 1.0
11–12	6.7 ± 0.4 ± 0.2 ± 0.9	5.9 ± 0.3 ± 0.1 ± 0.8	4.5 ± 0.3 ± 0.1 ± 0.6
12–13	4.6 ± 0.3 ± 0.2 ± 0.6	3.5 ± 0.2 ± 0.1 ± 0.5	2.9 ± 0.2 ± 0.1 ± 0.4
13–14	2.9 ± 0.3 ± 0.1 ± 0.4	2.6 ± 0.2 ± 0.1 ± 0.3	1.3 ± 0.2 ± 0.1 ± 0.2
	$3.5 < y < 4.0$	$4.0 < y < 4.5$	
0– 1	614 ± 6 ± 23 ± 81	447 ± 5 ± 28 ± 59	
1– 2	1101 ± 7 ± 23 ± 145	807 ± 7 ± 28 ± 107	
2– 3	839 ± 6 ± 19 ± 111	588 ± 6 ± 22 ± 78	
3– 4	471 ± 4 ± 13 ± 62	315 ± 4 ± 14 ± 42	
4– 5	244 ± 3 ± 7 ± 32	163 ± 3 ± 6 ± 22	
5– 6	119 ± 2 ± 5 ± 16	76 ± 2 ± 3 ± 10	
6– 7	59 ± 1 ± 2 ± 8	34 ± 1.1 ± 1.4 ± 4.5	
7– 8	29 ± 1 ± 1 ± 4	17 ± 0.7 ± 0.8 ± 2.3	
8– 9	15.9 ± 0.5 ± 0.1 ± 2.1	8.5 ± 0.5 ± 0.4 ± 1.1	
9–10	8.2 ± 0.4 ± 0.1 ± 1.1	4.1 ± 0.3 ± 0.2 ± 0.5	
10–11	4.9 ± 0.3 ± 0.1 ± 0.6	2.2 ± 0.2 ± 0.1 ± 0.3	
11–12	2.6 ± 0.2 ± 0.1 ± 0.3		
12–13	1.2 ± 0.1 ± 0.1 ± 0.2		

Table 5: $\frac{d^2\sigma}{dp_T dy}$ in nb/(GeV/c) for J/ψ from b in bins of the J/ψ transverse momentum and rapidity. The first error is statistical, the second is the component of the systematic uncertainty that is uncorrelated between bins and the third is the correlated component.

p_T (GeV/c)	$2.0 < y < 2.5$	$2.5 < y < 3.0$	$3.0 < y < 3.5$
0– 1	107 ± 23 ± 22 ± 15	75 ± 4 ± 12 ± 10	60 ± 2 ± 4 ± 8
1– 2	156 ± 11 ± 30 ± 22	147 ± 4 ± 4 ± 20	123 ± 3 ± 2 ± 17
2– 3	151 ± 6 ± 14 ± 21	140 ± 3 ± 3 ± 19	113 ± 2 ± 2 ± 16
3– 4	105 ± 4 ± 6 ± 15	98 ± 2 ± 2 ± 14	75 ± 2 ± 2 ± 10
4– 5	67 ± 2 ± 3 ± 9	57 ± 1 ± 2 ± 8	44 ± 1 ± 1 ± 6
5– 6	43 ± 2 ± 2 ± 6	35 ± 1 ± 1 ± 5	26 ± 1 ± 1 ± 4
6– 7	26 ± 1 ± 1 ± 4	22 ± 1 ± 1 ± 3	14.9 ± 0.6 ± 0.5 ± 2.1
7– 8	16.1 ± 0.7 ± 0.8 ± 2.2	12.1 ± 0.5 ± 0.6 ± 1.7	9.4 ± 0.4 ± 0.3 ± 1.3
8– 9	10.1 ± 0.6 ± 0.3 ± 1.4	8.2 ± 0.4 ± 0.8 ± 1.1	5.3 ± 0.3 ± 0.1 ± 0.7
9– 10	6.5 ± 0.4 ± 0.2 ± 0.9	5.2 ± 0.3 ± 0.1 ± 0.7	3.4 ± 0.2 ± 0.1 ± 0.5
10– 11	4.4 ± 0.3 ± 0.1 ± 0.6	3.2 ± 0.2 ± 0.1 ± 0.4	2.0 ± 0.2 ± 0.1 ± 0.3
11– 12	3.3 ± 0.3 ± 0.1 ± 0.4	2.2 ± 0.2 ± 0.1 ± 0.3	1.5 ± 0.2 ± 0.1 ± 0.2
12– 13	1.9 ± 0.2 ± 0.1 ± 0.3	1.6 ± 0.2 ± 0.1 ± 0.2	0.9 ± 0.1 ± 0.1 ± 0.1
13– 14	1.2 ± 0.2 ± 0.1 ± 0.2	0.9 ± 0.1 ± 0.1 ± 0.1	0.6 ± 0.1 ± 0.1 ± 0.1
	$3.5 < y < 4.0$	$4.0 < y < 4.5$	
0– 1	41 ± 2 ± 2 ± 6	22 ± 2 ± 1 ± 3	
1– 2	82 ± 2 ± 2 ± 11	52 ± 2 ± 2 ± 7	
2– 3	71 ± 2 ± 2 ± 10	42 ± 2 ± 2 ± 6	
3– 4	48 ± 1 ± 1 ± 7	28 ± 1 ± 1 ± 4	
4– 5	28 ± 1 ± 1 ± 4	15.0 ± 1.0 ± 0.6 ± 2.1	
5– 6	15.6 ± 0.7 ± 0.7 ± 2.2	9.0 ± 0.7 ± 0.3 ± 1.3	
6– 7	8.6 ± 0.4 ± 0.3 ± 1.2	5.2 ± 0.5 ± 0.2 ± 0.7	
7– 8	5.5 ± 0.3 ± 0.2 ± 0.8	2.8 ± 0.3 ± 0.1 ± 0.4	
8– 9	3.2 ± 0.3 ± 0.1 ± 0.4	1.5 ± 0.2 ± 0.1 ± 0.2	
9– 10	1.8 ± 0.2 ± 0.1 ± 0.2	0.8 ± 0.2 ± 0.1 ± 0.1	
10– 11	1.2 ± 0.2 ± 0.1 ± 0.2	0.5 ± 0.1 ± 0.1 ± 0.1	
11– 12	0.6 ± 0.1 ± 0.1 ± 0.1		
12– 13	0.3 ± 0.1 ± 0.1 ± 0.1		

Table 6: $\frac{d^2\sigma}{dp_T dy}$ in nb/(GeV/c) for prompt J/ψ in bins of the J/ψ transverse momentum and rapidity, assuming fully transversely polarised J/ψ . The first error is statistical, the second is the component of the systematic uncertainty that is uncorrelated between bins and the third is the correlated component.

p_T (GeV/c)	$2.0 < y < 2.5$	$2.5 < y < 3.0$	$3.0 < y < 3.5$
0– 1	1282 ± 83 ± 266 ± 169	1058 ± 16 ± 166 ± 140	924 ± 9 ± 56 ± 122
1– 2	1751 ± 44 ± 331 ± 231	1791 ± 15 ± 47 ± 236	1603 ± 10 ± 31 ± 212
2– 3	1438 ± 24 ± 129 ± 190	1423 ± 11 ± 28 ± 188	1182 ± 7 ± 21 ± 156
3– 4	932 ± 13 ± 53 ± 123	839 ± 7 ± 21 ± 111	675 ± 5 ± 15 ± 89
4– 5	513 ± 7 ± 27 ± 68	455 ± 4 ± 14 ± 60	358 ± 3 ± 10 ± 47
5– 6	278 ± 4 ± 15 ± 37	238 ± 3 ± 9 ± 32	184 ± 2 ± 6 ± 24
6– 7	140 ± 3 ± 7 ± 19	120 ± 2 ± 5 ± 16	91 ± 1 ± 3 ± 12
7– 8	76 ± 2 ± 4 ± 10	64 ± 1 ± 3 ± 8	49 ± 1 ± 2 ± 6
8– 9	44 ± 1 ± 1 ± 6	34 ± 1 ± 1 ± 5	25 ± 1 ± 1 ± 3
9–10	23 ± 1 ± 1 ± 3	19.3 ± 0.6 ± 0.2 ± 2.6	13.7 ± 0.5 ± 0.1 ± 1.8
10–11	13.5 ± 0.6 ± 0.4 ± 1.8	10.9 ± 0.4 ± 0.1 ± 1.4	8.5 ± 0.4 ± 0.1 ± 1.1
11–12	7.7 ± 0.4 ± 0.3 ± 1.0	6.4 ± 0.3 ± 0.1 ± 0.8	4.9 ± 0.3 ± 0.1 ± 0.6
12–13	5.2 ± 0.3 ± 0.2 ± 0.7	3.8 ± 0.3 ± 0.1 ± 0.5	3.1 ± 0.2 ± 0.1 ± 0.4
13–14	3.3 ± 0.3 ± 0.1 ± 0.4	2.8 ± 0.2 ± 0.1 ± 0.4	1.4 ± 0.2 ± 0.1 ± 0.2
	$3.5 < y < 4.0$	$4.0 < y < 4.5$	
0– 1	728 ± 7 ± 27 ± 96	530 ± 6 ± 33 ± 70	
1– 2	1246 ± 8 ± 26 ± 164	902 ± 7 ± 31 ± 119	
2– 3	913 ± 6 ± 21 ± 120	631 ± 6 ± 24 ± 83	
3– 4	505 ± 4 ± 14 ± 67	334 ± 4 ± 15 ± 44	
4– 5	262 ± 3 ± 8 ± 35	172 ± 3 ± 7 ± 23	
5– 6	128 ± 2 ± 5 ± 17	79 ± 2 ± 3 ± 11	
6– 7	63 ± 1 ± 2 ± 8	36 ± 1 ± 2 ± 5	
7– 8	32 ± 1 ± 1 ± 4	18.3 ± 0.7 ± 0.8 ± 2.4	
8– 9	17.1 ± 0.6 ± 0.2 ± 2.3	8.9 ± 0.5 ± 0.4 ± 1.2	
9–10	8.8 ± 0.4 ± 0.1 ± 1.2	4.3 ± 0.3 ± 0.2 ± 0.5	
10–11	5.2 ± 0.3 ± 0.1 ± 0.7	2.4 ± 0.2 ± 0.1 ± 0.3	
11–12	2.8 ± 0.2 ± 0.1 ± 0.4		
12–13	1.3 ± 0.1 ± 0.1 ± 0.2		

Table 7: $\frac{d^2\sigma}{dp_T dy}$ in nb/(GeV/c) for prompt J/ψ in bins of the J/ψ transverse momentum and rapidity, assuming fully longitudinally polarised J/ψ . The first error is statistical, the second is the component of the systematic uncertainty that is uncorrelated between bins and the third is the correlated component.

p_T (GeV/c)	$2.0 < y < 2.5$	$2.5 < y < 3.0$	$3.0 < y < 3.5$
0– 1	$839 \pm 54 \pm 174 \pm 111$	$601 \pm 9 \pm 94 \pm 79$	$543 \pm 5 \pm 33 \pm 72$
1– 2	$1157 \pm 29 \pm 219 \pm 153$	$1114 \pm 9 \pm 29 \pm 147$	$1073 \pm 7 \pm 21 \pm 142$
2– 3	$945 \pm 16 \pm 84 \pm 125$	$938 \pm 7 \pm 19 \pm 124$	$865 \pm 5 \pm 16 \pm 114$
3– 4	$583 \pm 8 \pm 33 \pm 77$	$559 \pm 4 \pm 14 \pm 74$	$514 \pm 4 \pm 11 \pm 68$
4– 5	$315 \pm 4 \pm 16 \pm 42$	$307 \pm 3 \pm 9 \pm 41$	$274 \pm 2 \pm 8 \pm 36$
5– 6	$171 \pm 3 \pm 9 \pm 23$	$163 \pm 2 \pm 6 \pm 22$	$140 \pm 2 \pm 4 \pm 19$
6– 7	$87 \pm 2 \pm 5 \pm 12$	$83 \pm 1 \pm 3 \pm 11$	$70 \pm 1 \pm 3 \pm 9$
7– 8	$48 \pm 1 \pm 2 \pm 6$	$46 \pm 1 \pm 2 \pm 6$	$38 \pm 1 \pm 1 \pm 5$
8– 9	$29 \pm 1 \pm 1 \pm 4$	$25 \pm 1 \pm 1 \pm 3$	$19.8 \pm 0.5 \pm 0.1 \pm 2.6$
9–10	$14.9 \pm 0.5 \pm 0.4 \pm 2.0$	$14.5 \pm 0.4 \pm 0.2 \pm 1.9$	$10.8 \pm 0.4 \pm 0.1 \pm 1.4$
10–11	$9.1 \pm 0.4 \pm 0.3 \pm 1.2$	$8.3 \pm 0.3 \pm 0.1 \pm 1.1$	$6.7 \pm 0.3 \pm 0.1 \pm 0.9$
11–12	$5.3 \pm 0.3 \pm 0.2 \pm 0.7$	$5.0 \pm 0.3 \pm 0.1 \pm 0.7$	$4.0 \pm 0.2 \pm 0.1 \pm 0.5$
12–13	$3.7 \pm 0.2 \pm 0.1 \pm 0.5$	$3.0 \pm 0.2 \pm 0.1 \pm 0.4$	$2.5 \pm 0.2 \pm 0.1 \pm 0.4$
13–14	$2.3 \pm 0.2 \pm 0.1 \pm 0.3$	$2.3 \pm 0.2 \pm 0.1 \pm 0.3$	$1.2 \pm 0.1 \pm 0.1 \pm 0.2$
	$3.5 < y < 4.0$	$4.0 < y < 4.5$	
0– 1	$468 \pm 4 \pm 21 \pm 62$	$341 \pm 4 \pm 21 \pm 45$	
1– 2	$892 \pm 5 \pm 18 \pm 118$	$667 \pm 6 \pm 23 \pm 88$	
2– 3	$721 \pm 5 \pm 16 \pm 95$	$517 \pm 5 \pm 20 \pm 68$	
3– 4	$415 \pm 3 \pm 12 \pm 55$	$282 \pm 4 \pm 13 \pm 37$	
4– 5	$215 \pm 2 \pm 7 \pm 28$	$148 \pm 2 \pm 6 \pm 20$	
5– 6	$104 \pm 1 \pm 4 \pm 14$	$69 \pm 2 \pm 3 \pm 9$	
6– 7	$51 \pm 1 \pm 2 \pm 7$	$31 \pm 1 \pm 1 \pm 4$	
7– 8	$26 \pm 1 \pm 1 \pm 3$	$15.8 \pm 0.6 \pm 0.7 \pm 2.1$	
8– 9	$13.9 \pm 0.5 \pm 0.1 \pm 1.8$	$7.6 \pm 0.4 \pm 0.3 \pm 1.0$	
9–10	$7.1 \pm 0.3 \pm 0.1 \pm 0.9$	$3.6 \pm 0.3 \pm 0.2 \pm 0.5$	
10–11	$4.3 \pm 0.2 \pm 0.1 \pm 0.6$	$2.0 \pm 0.2 \pm 0.1 \pm 0.3$	
11–12	$2.3 \pm 0.2 \pm 0.1 \pm 0.3$		
12–13	$1.0 \pm 0.1 \pm 0.1 \pm 0.1$		

Table 8: Fraction of J/ψ from b (in %) in bins of the J/ψ transverse momentum and rapidity. The first uncertainty is statistical, the second systematic (uncorrelated between bins) and the third is the uncertainty due to the unknown polarisation of the prompt J/ψ ; the central values are for unpolarised J/ψ .

p_T (GeV/c)	$2.0 < y < 2.5$	$2.5 < y < 3.0$	$3.0 < y < 3.5$
0– 1	$8.9 \pm 1.7 \pm 0.3^{+1.2}_{-2.4}$	$8.2 \pm 0.4 \pm 0.3^{+1.5}_{-2.9}$	$7.4 \pm 0.3 \pm 0.3^{+1.3}_{-2.5}$
1– 2	$9.4 \pm 0.7 \pm 0.3^{+1.3}_{-2.4}$	$9.0 \pm 0.2 \pm 0.3^{+1.4}_{-2.7}$	$8.2 \pm 0.2 \pm 0.3^{+1.1}_{-2.1}$
2– 3	$11.0 \pm 0.5 \pm 0.4^{+1.5}_{-2.8}$	$10.3 \pm 0.2 \pm 0.4^{+1.4}_{-2.6}$	$9.7 \pm 0.2 \pm 0.3^{+1.0}_{-1.9}$
3– 4	$11.9 \pm 0.4 \pm 0.4^{+1.8}_{-3.3}$	$12.0 \pm 0.2 \pm 0.4^{+1.5}_{-2.9}$	$11.0 \pm 0.2 \pm 0.4^{+0.9}_{-1.8}$
4– 5	$13.6 \pm 0.4 \pm 0.5^{+2.1}_{-3.9}$	$12.7 \pm 0.3 \pm 0.5^{+1.6}_{-3.0}$	$11.9 \pm 0.3 \pm 0.4^{+1.0}_{-1.9}$
5– 6	$15.7 \pm 0.5 \pm 0.6^{+2.4}_{-4.3}$	$14.6 \pm 0.4 \pm 0.5^{+1.7}_{-3.2}$	$13.6 \pm 0.4 \pm 0.5^{+1.1}_{-2.1}$
6– 7	$18.4 \pm 0.7 \pm 0.7^{+2.6}_{-4.8}$	$17.5 \pm 0.5 \pm 0.6^{+1.9}_{-3.5}$	$15.4 \pm 0.5 \pm 0.6^{+1.2}_{-2.3}$
7– 8	$20.1 \pm 0.8 \pm 0.7^{+2.6}_{-4.8}$	$17.6 \pm 0.7 \pm 0.6^{+1.8}_{-3.4}$	$17.8 \pm 0.7 \pm 0.6^{+1.3}_{-2.5}$
8– 9	$21.4 \pm 1.0 \pm 0.8^{+2.6}_{-4.7}$	$21.2 \pm 0.9 \pm 0.8^{+1.9}_{-3.5}$	$18.6 \pm 1.0 \pm 0.7^{+1.4}_{-2.6}$
9–10	$25.3 \pm 1.4 \pm 0.9^{+2.8}_{-5.1}$	$23.1 \pm 1.2 \pm 0.8^{+1.8}_{-3.4}$	$21.5 \pm 1.3 \pm 0.8^{+1.3}_{-2.5}$
10–11	$27.6 \pm 1.7 \pm 1.0^{+2.9}_{-5.2}$	$24.6 \pm 1.5 \pm 0.9^{+1.8}_{-3.3}$	$20.2 \pm 1.7 \pm 0.7^{+1.3}_{-2.5}$
11–12	$32.8 \pm 2.2 \pm 1.2^{+2.9}_{-5.2}$	$27.0 \pm 2.0 \pm 1.0^{+1.8}_{-3.3}$	$24.7 \pm 2.2 \pm 0.9^{+1.3}_{-2.4}$
12–13	$28.9 \pm 2.6 \pm 1.0^{+2.6}_{-4.7}$	$31.3 \pm 2.6 \pm 1.1^{+1.9}_{-3.5}$	$24.1 \pm 2.8 \pm 0.9^{+1.3}_{-2.4}$
13–14	$29.8 \pm 3.6 \pm 1.1^{+2.6}_{-4.8}$	$26.5 \pm 2.9 \pm 1.0^{+1.5}_{-2.8}$	$32.5 \pm 4.1 \pm 1.2^{+1.5}_{-2.8}$
	$3.5 < y < 4.0$	$4.0 < y < 4.5$	
0– 1	$6.3 \pm 0.3 \pm 0.2^{+0.9}_{-1.8}$	$4.8 \pm 0.4 \pm 0.2^{+0.7}_{-1.4}$	
1– 2	$6.9 \pm 0.2 \pm 0.2^{+0.8}_{-1.5}$	$6.1 \pm 0.2 \pm 0.2^{+0.6}_{-1.2}$	
2– 3	$7.9 \pm 0.2 \pm 0.3^{+0.6}_{-1.2}$	$6.7 \pm 0.3 \pm 0.2^{+0.4}_{-0.9}$	
3– 4	$9.3 \pm 0.3 \pm 0.3^{+0.6}_{-1.1}$	$8.1 \pm 0.4 \pm 0.3^{+0.4}_{-0.9}$	
4– 5	$10.2 \pm 0.3 \pm 0.4^{+0.6}_{-1.2}$	$8.4 \pm 0.5 \pm 0.3^{+0.4}_{-0.8}$	
5– 6	$11.6 \pm 0.5 \pm 0.4^{+0.7}_{-1.4}$	$10.7 \pm 0.7 \pm 0.4^{+0.4}_{-0.9}$	
6– 7	$12.7 \pm 0.6 \pm 0.5^{+0.8}_{-1.6}$	$13.3 \pm 1.1 \pm 0.5^{+0.5}_{-1.1}$	
7– 8	$15.7 \pm 0.9 \pm 0.6^{+1.0}_{-1.9}$	$13.7 \pm 1.4 \pm 0.5^{+0.6}_{-1.2}$	
8– 9	$16.6 \pm 1.2 \pm 0.6^{+1.0}_{-2.0}$	$15.2 \pm 2.0 \pm 0.5^{+0.7}_{-1.4}$	
9–10	$18.0 \pm 1.6 \pm 0.6^{+1.1}_{-2.1}$	$17.0 \pm 2.9 \pm 0.6^{+0.9}_{-1.7}$	
10–11	$19.8 \pm 2.2 \pm 0.7^{+1.1}_{-2.1}$	$17.7 \pm 3.9 \pm 0.6^{+0.8}_{-1.6}$	
11–12	$19.5 \pm 2.9 \pm 0.8^{+1.1}_{-2.0}$		
12–13	$21.9 \pm 4.4 \pm 0.8^{+1.2}_{-2.4}$		